

This is a repository copy of *The CLAS12 Spectrometer at Jefferson Laboratory*.

White Rose Research Online URL for this paper:
<https://eprints.whiterose.ac.uk/157263/>

Version: Accepted Version

Article:

Burkert, V. D., Elouadrhiri, L., Adhikari, K. P. et al. (200 more authors) (2020) The CLAS12 Spectrometer at Jefferson Laboratory. *Nuclear Instruments and Methods in Physics Research, Section A: Accelerators, Spectrometers, Detectors and Associated Equipment*. 163419. ISSN 0168-9002

<https://doi.org/10.1016/j.nima.2020.163419>

Reuse

This article is distributed under the terms of the Creative Commons Attribution-NonCommercial-NoDerivs (CC BY-NC-ND) licence. This licence only allows you to download this work and share it with others as long as you credit the authors, but you can't change the article in any way or use it commercially. More information and the full terms of the licence here: <https://creativecommons.org/licenses/>

Takedown

If you consider content in White Rose Research Online to be in breach of UK law, please notify us by emailing eprints@whiterose.ac.uk including the URL of the record and the reason for the withdrawal request.

The CLAS12 Spectrometer at Jefferson Laboratory

V.D. Burkert^{am}, L. Elouadrhiri^{am}, K.P. Adhikari^{aa}, S. Adhikari^l, M.J. Amaryan^{af}, D. Anderson^{am}, G. Angelini^m, H. Atac^{al}, S. Aune^d, H. Avakian^{am}, C. Ayerbe Gayoso^{at,aa}, N. Baltzell^{am}, L. Barion^o, M. Battaglieri^{q,am}, V. Baturin^{am}, I. Bedlinskiy^{ab}, F. Benmokhtar^h, A. Bianconi^{ap,t}, A.S. Biselli^j, F. Bossù^d, S. Boyarinov^{am}, W.J. Briscoe^m, W.K. Brooks^{an}, K. Bruhwel^{am}, D.S. Carman^{am}, A. Celentano^q, G. Charles^{u,af}, P. Chatagnon^u, S. Christo^{am}, T. Chetry^{aa,ae}, G. Christiaens^{aq,d}, G. Ciullo^{o,k}, B.A. Clary^f, P.L. Coleyⁿ, M. Contalbrigo^o, R. Cruz-Torres^z, C. Cuevas^{am}, A. D'Angelo^{r,ai}, N. Dashyan^{au}, R. De Vita^q, M. Defurne^d, A. Deur^{am}, S. Diehl^f, C. Djalali^{ae,ak}, G. Dodge^{af}, R. Dupre^u, M. Ehrhart^{a,u}, L. El Fassi^{aa}, R. Fair^{am}, G. Fedotov^{ae}, A. Filippi^s, T.A. Forestⁿ, M. Garçon^d, G. Gavalian^{am}, G.P. Gilfoyle^{ah}, K. Giovanetti^w, F.X. Girod^{am}, D.I. Glazier^{aq}, E. Golovatch^{aj}, R.W. Gothe^{ak}, Y. Gotra^{am}, K.A. Griffioen^{at}, M. Guidal^u, K. Hafidi^a, H. Hakobyan^{an,au}, C. Hanretty^{am}, N. Harrison^{am}, M. Hattawy^{af,a}, F. Hauenstein^{af}, T.B. Hayward^{at}, D. Heddle^{e,am}, P. Hemler^{am}, O.A. Hen^z, K. Hicks^{ae}, A. Hobart^u, M. Holtrop^{ac}, Y. Ilieva^{ak}, I. Illari^m, D. Insley^{am}, D.G. Ireland^{aq}, B.S. Ishkhanov^{aj}, E.L. Isupov^{aj}, H.S. Jo^x, K. Joo^f, S. Joosten^{a,al}, T. Kageya^{am}, D. Kashy^{am}, C. Keith^{am}, D. Keller^{as}, M. Khachatryan^{af}, A. Khanal^l, A. Kim^f, C.W. Kim^m, W. Kim^x, V. Kubarovsky^{am}, S.E. Kuhn^{af}, L. Lanza^r, A. Lung^{am}, M.L. Kabir^{aa}, M. Leali^{ap,t}, P. Lenisa^o, K. Livingston^{aq}, M. Lowry^{am}, I. J.D. MacGregor^{aq}, I. Mandjavidze^d, D. Marchand^u, N. Markov^f, V. Mascagna^{ao,t,ap}, B. McKinnon^{aq}, M. McMullen^{am}, C. Mealer^{am}, M.D. Mestayer^{am}, Z.E. Meziani^{a,al}, R. Miller^{am}, T. Mineeva^{an}, M. Mirazita^P, V. Mokeev^{am}, A. Movsisyan^o, C. Munoz Camacho^u, P. Naidoo^{aq}, S. Nanda^{aa}, J. Newton^{af}, S. Niccolai^u, G. Niculescu^w, M. Osipenko^q, M. Paolone^{al}, L.L. Pappalardo^o, R. Paremuzyan^{ac}, O. Pastor^{am}, E. Pasyuk^{am}, W. Phelps^{e,m}, O. Pogorelko^{ab}, J. Poudel^{af}, J.W. Price^b, K. Price^u, Y. Prok^{af}, B.A. Rau^{l,am}, M. Ripani^q, J. Ritman^v, A. Rizzo^{r,ai}, G. Rosner^{aq}, P. Rossi^{am}, J. Rowley^{ae}, B.J. Roy^v, F. Sabatié^d, C. Salgado^{ad}, S. Schadmand^v, A. Schmidt^{z,m}, E.P. Segarra^z, V. Sergeyeva^u, Y.G. Sharabian^{am}, U. Shrestha^{ae}, Iu. Skorodumina^{ak,aj}, G.D. Smithⁱ, L.C. Smith^{as,am}, D. Sokhan^{aq}, O. Soto^{p,an}, N. Sparveris^{al}, S. Stepanyan^{am}, P. Stoler^{ag}, S. Strauch^{ak}, J.A. Tan^x, D. Tilles^{am}, M. Turisini^P, N. Tyler^{ak}, M. Ungaro^{am}, L. Venturelli^{ap,t}, H. Voskanyan^{au}, E. Voutier^u, D. Watts^{ar}, X. Wei^{am}, L.B. Weinstein^{af}, C. Wiggins^{am}, M.H. Wood^c, A. Yegneswaran^{am}, G. Young^{am}, N. Zachariou^{ar}, M. Zarecky^{am}, J. Zhang^{as}, Z.W. Zhao^{g,af}, V. Ziegler^{am}

^aArgonne National Laboratory, Argonne, Illinois 60439

^bCalifornia State University, Dominguez Hills, Carson, CA 90747

^cCanisius College, Buffalo, NY 14208

^dIRFU, CEA, Université Paris-Saclay, F-91191 Gif-sur-Yvette, France

^eChristopher Newport University, Newport News, Virginia 23606

^fUniversity of Connecticut, Storrs, Connecticut 06269

^gDuke University, Durham, North Carolina 27708

^hDuquesne University, Pittsburgh, PA 15282

ⁱEdinburgh University, Edinburgh EH9 3JZ, United Kingdom

^jFairfield University, Fairfield CT 06424

^kUniversità' di Ferrara , 44121 Ferrara, Italy

^lFlorida International University, Miami, Florida 33199

^mThe George Washington University, Washington, DC 20052

ⁿIdaho State University, Pocatello, Idaho 83209

^oINFN, Sezione di Ferrara, 44100 Ferrara, Italy

^pINFN, Laboratori Nazionali di Frascati, 00044 Frascati, Italy

^qINFN, Sezione di Genova, 16146 Genova, Italy

^rINFN, Sezione di Roma Tor Vergata, 00133 Rome, Italy

^sINFN, Sezione di Torino, 10125 Torino, Italy

^tINFN, Sezione di Pavia, 27100 Pavia, Italy

^uInstitut de Physique Nucléaire, IN2P3-CNRS, Université Paris-Sud, Université Paris-Saclay, F-91406 Orsay, France

^vInstitute fur Kernphysik (Juelich), 52428 Juelich, Germany

^wJames Madison University, Harrisonburg, Virginia 22807

^xKyungpook National University, Daegu 41566, Republic of Korea

^yLamar University, Beaumont, Texas 77710

^zMassachusetts Institute of Technology, Cambridge, Massachusetts 02139

^{aa}Mississippi State University, Mississippi State, MS 39762

^{ab}National Research Centre Kurchatov Institute - ITEP, Moscow, 117259, Russia

56 ^{ac}*University of New Hampshire, Durham, New Hampshire 03824*
57 ^{ad}*Norfolk State University, Norfolk, Virginia 23504*
58 ^{ae}*Ohio University, Athens, Ohio 45701*
59 ^{af}*Old Dominion University, Norfolk, Virginia 23529*
60 ^{ag}*Rensselaer Polytechnic Institute, Troy, New York 12180*
61 ^{ah}*University of Richmond, Richmond, Virginia 23173*
62 ^{ai}*Universita' di Roma Tor Vergata, 00133 Rome Italy*
63 ^{aj}*Skobeltsyn Institute of Nuclear Physics, Lomonosov Moscow State University, 119234 Moscow, Russia*
64 ^{ak}*University of South Carolina, Columbia, South Carolina 29208*
65 ^{al}*Temple University, Philadelphia, PA 19122*
66 ^{am}*Thomas Jefferson National Accelerator Facility, Newport News, Virginia 23606*
67 ^{an}*Universidad Técnica Federico Santa María, Casilla 110-V Valparaíso, Chile*
68 ^{ao}*Università degli Studi dell'Insubria, 22100 Como, Italy*
69 ^{ap}*Università degli Studi di Brescia, 25123 Brescia, Italy*
70 ^{aq}*University of Glasgow, Glasgow G12 8QQ, United Kingdom*
71 ^{ar}*University of York, York YO10 5DD, United Kingdom*
72 ^{as}*University of Virginia, Charlottesville, Virginia 22901*
73 ^{at}*College of William and Mary, Williamsburg, Virginia 23187*
74 ^{au}*Yerevan Physics Institute, 375036 Yerevan, Armenia*

75 **Abstract**

The CEBAF Large Acceptance Spectrometer for operation at 12 GeV beam energy (CLAS12) in Hall B at Jefferson Laboratory is used to study electro-induced nuclear and hadronic reactions. This spectrometer provides efficient detection of charged and neutral particles over a large fraction of the full solid angle. CLAS12 has been part of the energy-doubling project of Jefferson Lab's Continuous Electron Beam Accelerator Facility, funded by the United States Department of Energy. An international collaboration of over 40 institutions contributed to the design and construction of detector hardware, developed the software packages for the simulation of complex event patterns, and commissioned the detector systems. CLAS12 is based on a dual-magnet system with a superconducting torus magnet that provides a largely azimuthal field distribution that covers the forward polar angle range up to 35°, and a solenoid magnet and detector covering the polar angles from 35° to 125° with full azimuthal coverage. Trajectory reconstruction in the forward direction using drift chambers and in the central direction using a vertex tracker results in momentum resolutions of <1% and <3%, respectively. Cherenkov counters, time-of-flight scintillators, and electromagnetic calorimeters provide good particle identification. Fast triggering and high data-acquisition rates allow operation at a luminosity of $10^{35} \text{ cm}^{-2}\text{s}^{-1}$. These capabilities are being used in a broad program to study the structure and interactions of nucleons, nuclei, and mesons, using polarized and unpolarized electron beams and targets for beam energies up to 11 GeV. This paper gives a general description of the design, construction, and performance of CLAS12.

76 Keywords: CLAS12, Magnetic spectrometer, Elec-
77 tromagnetic physics, Large Acceptance, JLab

78 1. Introduction

79 Electron scattering has proven an effective way
80 of probing the size and internal structure of sub-
81 atomic particles such as protons, neutrons, and nu-
82 clei. Exploiting energetic electron beams led to
83 rapid progress in our understanding of the internal
84 composition of particles. The extended size of the
85 proton was first mapped out in the mid-1950's [1],
86 and the internal quark substructure was discovered
87 in the late 1960's [2]. Using spin-polarized elec-
88 trons and spin-polarized targets, the internal quark
89 helicity momentum distribution was mapped out in
90 the 1980's and the following decades, and is still an
91 important research topic today [3]. These experi-
92 ments required only inclusive measurements, where
93 only the beam particle, electrons or muons, that
94 scattered off the target were detected and kinemat-
95 ically analyzed.

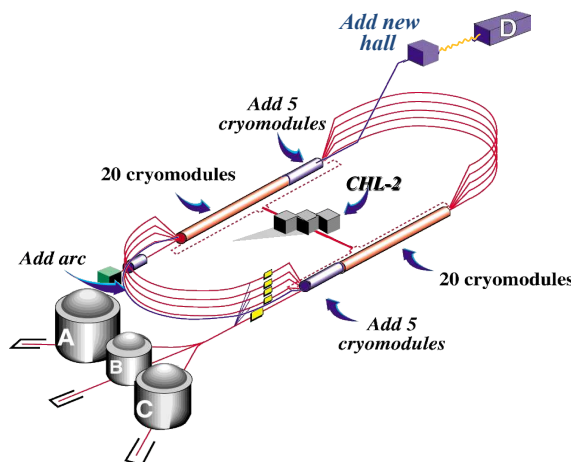


Figure 1: The CEBAF continuous electron beam accelerator after the doubling of the beam energy to 12 GeV and adding Hall D as a new experimental end station for photon physics experiments. The accelerator is 1,400 m in circumference.

96 In the decades following these discoveries, it was
97 realized that a more detailed understanding of the
98 internal structure of nucleons requires the recon-
99 struction of fully exclusive or semi-inclusive pro-
100 cesses, and hence the detection and kinematical re-
101 construction of additional mesons and baryons in
102 the final state was required. Other constraints came
103 from the need of baryon spectroscopy to measure

104 complete angular distributions, which made it nec-
105 essary to employ large acceptance devices to serve
106 that purpose. The Continuous Electron Beam Ac-
107 celerator Facility (CEBAF) [4], the CLAS detec-
108 tor [5], and other experimental equipment at Jef-
109 ferson Laboratory (JLab) were designed and con-
110 structed in the 1990's with these goals in mind and
111 were operated successfully for over 15 years.

112 The further development of Quantum Chromo-
113 dynamics (QCD) as the theory of the interaction
114 of colored quarks and gluons, combined with the
115 discovery of the Generalized Parton Distributions
116 (GPDs), provided a novel way that allowed describ-
117 ing the nucleon structure in 3 dimensions (3D), 2 in
118 coordinate space and 1 in momentum space. The
119 discovery opened up a new avenue of hadronic re-
120 search that has become one of the flagship programs
121 in nuclear and hadronic physics. The GPDs must
122 be probed in exclusive processes, with deeply virtual
123 Compton scattering being the most suitable one.
124 This is a rather rare process and measurements
125 require the operation of large acceptance detectors
126 at high instantaneous luminosities of $10^{35} \text{ cm}^{-2}\text{s}^{-1}$
127 to map out the process in the full kinematic phase
128 space using polarized beams, polarized targets, and
129 sufficiently high beam energy. The complementary
130 process of semi-inclusive deep inelastic scattering
131 (SIDIS) is also of topical interest to probe the in-
132 ternal structure of the nucleon in 3D momentum
133 space. The science program of CLAS12 is very
134 broad [6] and encompasses the study of the struc-
135 ture of the proton and neutron both in their ground
136 state, as well as their many excited states, and in
137 the deeply inelastic kinematics. Other experiments
138 are designed to probe the short range structure of
139 nuclei through measurements of the transparency of
140 nuclei to mesons and baryons, and how it changes
141 with the momentum transfer.

142 2. The JLab Facility at 12 GeV

143 The CLAS12 detector was designed to study
144 electro-induced nuclear and hadronic reactions by
145 providing efficient detection of charged and neutral
146 particles over a large fraction of the full solid an-
147 gle. A collaboration of over 40 institutions has par-
148 participated in the design, fabrication, assembly, and
149 final commissioning of CLAS12 in Hall B at Jef-
150 ferson Laboratory. The CLAS12 detector is based
151 on a combination of a six-coil torus magnet and a
152 high-field solenoid magnet. The combined magnetic
153 field provides a large coverage in both azimuthal

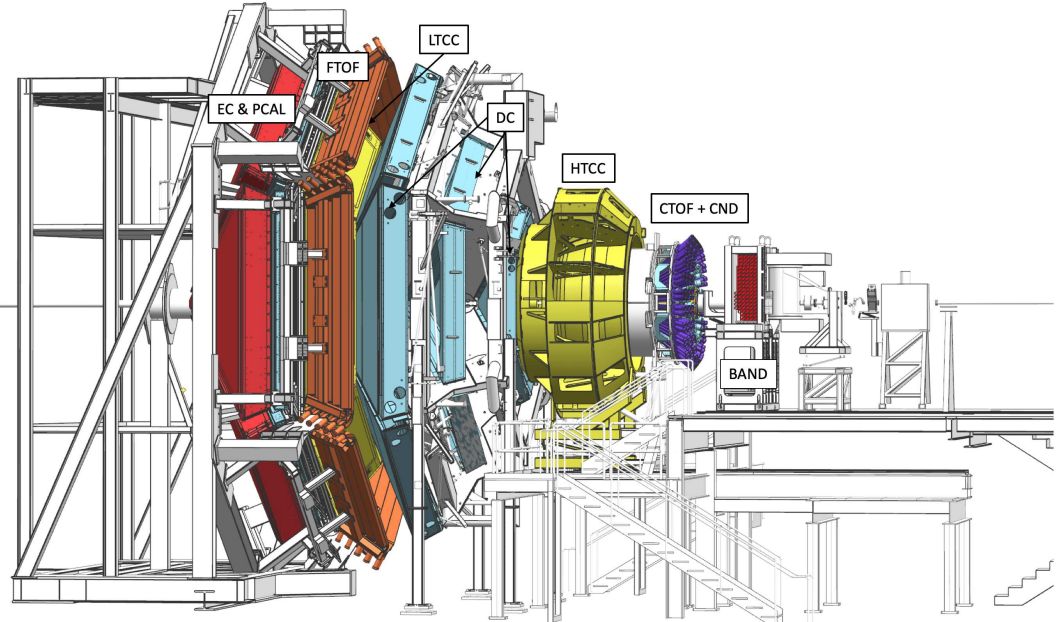


Figure 2: The CLAS12 detector in the Hall B beamline. The electron beam enters from the right and impinges on the production target located in the center of the solenoid magnet shown at the right (upstream) end of CLAS12, where other detector components are also visible. Scattered electrons and forward-going particles are detected in the Forward Detector (FD) consisting of the High Threshold Cherenkov Counter (HTCC) (yellow) with full coverage in polar angle $5^\circ \leq \theta \leq 35^\circ$ and $\Delta\phi = 2\pi$ coverage in azimuth. The HTCC is followed by the torus magnet (gray), the drift chamber tracking system (light blue), another set of Cherenkov counters (hidden), time-of-flight scintillation counters (brown), and electromagnetic calorimeters (red). Between the HTCC and the torus, the Forward Tagger is installed to detect electrons and photons at polar angles $2^\circ \leq \theta \leq 5^\circ$. The Central Detector (CD) consists of the Silicon Vertex Tracker (hidden), which is surrounded by a Barrel Micromesh Tracker (hidden), the Central Time-of-Flight system, and the Central Neutron Detector (PMTs in blue). At the upstream end, a Back Angle Neutron Detector (red) is installed. In the operational configuration, the entire CLAS12 detector extends for 13 m along the beamline.

and polar angles. Trajectory reconstruction using drift chambers at forward angles results in a momentum resolution of $\sigma_p/p \approx 0.7\%$. At large polar angles, where particle momenta are typically below 1 GeV, the momentum resolution is $\sigma_p/p \approx 3.5\%$. Cherenkov counters, time-of-flight systems, and calorimeters provide good particle identification for electrons, charged pions, kaons, and protons. Fast triggering and high data acquisition rates allow operation at luminosities of $10^{35} \text{ cm}^{-2}\text{s}^{-1}$ for extended periods of time. These capabilities are being used in a broad scientific program to study the structure and interactions of baryons, mesons, and nuclei using polarized and unpolarized targets.

This paper provides a general description of the design, construction, and performance of CLAS12 and how it expands upon the capabilities provided by the JLab 12 GeV energy upgrade. The CEBAF accelerator and experimental halls are shown for the energy upgraded configuration in Fig. 1. CEBAF is designed from two parallel linear acceler-

ators (linacs) based on superconducting radio frequency (RF) technology, and arranged in a race-track configuration [4]. Spin-polarized electrons are generated in the gun, pre-accelerated in the injector, and subsequently injected and accelerated in the north linac. They are then bent in a 180° arc and injected into the south linac. This is repeated four and a half more times to reach the final energy for Hall D and up to four times for the desired delivery energies to Halls A, B, and C. In the recirculating arcs, electrons are transported in 5 independent out-of-phase tracks of different energies. For 12 GeV operation, five accelerating cryomodules with four times higher gradients than were used in the 6 GeV CEBAF machine were added to each of the two existing linacs to reach a maximum energy of 11 GeV for Halls A, B, and C. One added arc path and one more pass through the north linac were added to achieve the highest beam energy of 12 GeV for Hall D. This highest beam energy is generated exclusively for Hall D, while the other three

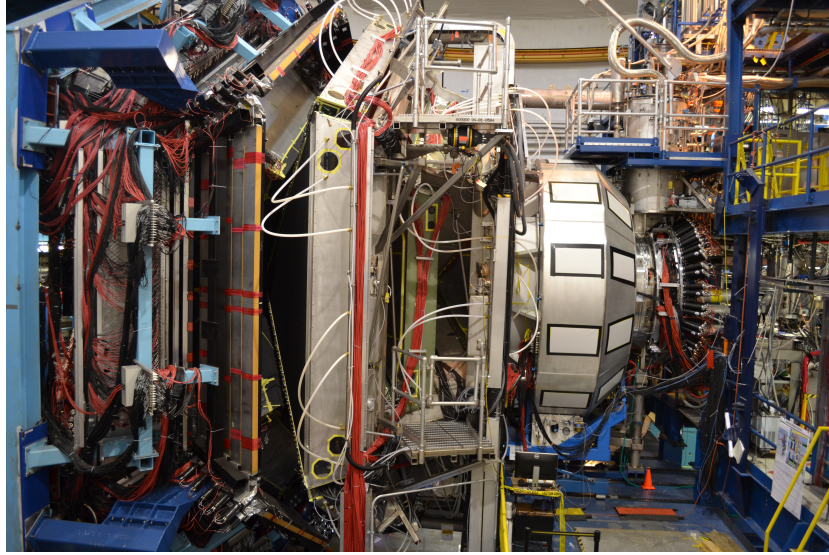


Figure 3: The CLAS12 detector in the Hall B beamline. The beam enters from the right near the upstream end of the solenoid magnet and the cryogenic service tower, followed by the HTCC and the torus magnet with the drift chambers. The Low Threshold Cherenkov Counter, Forward Time-of-Flight, and the electromagnetic calorimeters (PCAL and EC) are seen at the downstream end to the left.



Figure 4: The CLAS12 magnet systems. Left: The fully assembled solenoid magnet including all cryogenic connections on the beamline at the beginning of cool down, before the detector installation. Right: The torus magnet with all six coils mechanically assembled in a common cryostat. The coil cryostat, which is fabricated from non-magnetic steel, has an outside width of 124 mm. The cross bars provide a cold (4.5 K) cryogenic connection of neighboring coils, and counteract the out-of-plane forces to provide mechanical stability to the full magnet. Due to the large physical size of the assembled torus magnet, the final assembly of the magnet had to be completed in Hall B.

¹⁹⁶ halls may receive beams at the same beam energy ¹⁹⁷ or at different beam energies simultaneously, with

¹⁹⁸ up to a factor of 10^5 differences in current from 1 nA
¹⁹⁹ to 100 μ A.

²⁰⁰ Major new detectors and other experimental equipment have been installed in Halls B, C, and D that
²⁰¹ support a broad science program addressing fundamental issues in nuclear and hadronic physics. In
²⁰² Hall D, a large hermetic detector with a solenoid
²⁰³ magnet at its core has been in operation since 2015.
²⁰⁴ It incorporates tracking capabilities and photon detection over nearly the full 4π solid angle. This hall is dedicated to the production of mesons employing a linearly polarized photon beam. The new
²⁰⁵ CLAS12 spectrometer, displayed in a side view in
²⁰⁶ Fig. 2 (from the design model) and in Fig. 3 (photograph), features large solid angle coverage and instantaneou
²⁰⁷s luminosities of 10^{35} $\text{cm}^{-2}\text{s}^{-1}$ for electron scattering experiments with multiple particle final states.

²¹⁶ Hall C includes the new super-high momentum magnetic spectrometer (SHMS) in addition to the existing high momentum spectrometer. In Hall A,
²¹⁷ a new super big bite spectrometer (SBS) has been added to the existing high resolution spectrometer pair HRS², and other large installation experiments have been proposed. Complementing the new equipment is the highly spin-polarized electron gun, high-power cryogenic targets, and several spin-polarized targets using NH₃, ND₃, HD, ³He, and ⁷Li as target materials to support a broad range of polarization measurements.

²²⁸ 3. The CLAS12 Superconducting Magnets

²²⁹ The design of CLAS12 is based on a combination of a toroidal magnetic field at polar angles up to $\approx 35^\circ$ and a 5 T solenoidal field in the central region in the approximate polar angle range $35^\circ \leq \theta \leq 125^\circ$. The primary requirement driving this choice is the ability to measure charged particles at high momentum with good resolution at forward angles, while operating the detector systems at high luminosity. This requires effective shielding of the detector system from low-energy electrons produced in the target material due to Møller scattering $e^- + e^- \rightarrow e^- + e^-$ of the high-energy beam electrons on atomic electrons in the target material. The large majority of those electrons are prevented from reaching the sensitive detectors as they curl up in the strong longitudinal magnetic field, and are then guided into a shielding pipe made from bulk tungsten material where they dump their en-

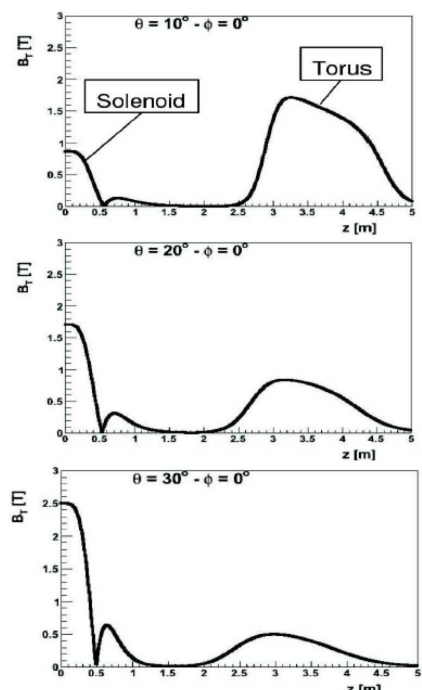


Figure 5: Combined solenoid and torus magnetic fields, showing the magnetic field component perpendicular to the radial distance from the solenoid center. Only the transverse components act on the charged tracks. At small polar angles the particle deflecting component is small in the solenoid field, while it is largest in the torus magnet. For large polar angle the transverse component is large in the solenoid field and small in the torus field volume.

247 ergy. The fully assembled torus and solenoid mag-
248 nets are shown in Fig. 4.

249 The distribution of the absolute magnetic field
250 along lines of constant polar angle seen from the
251 target position is shown in Fig. 5. Both the torus
252 and solenoid magnetic fields are included. The field
253 distributions of the solenoid and torus magnets are
254 shown in Fig. 6.

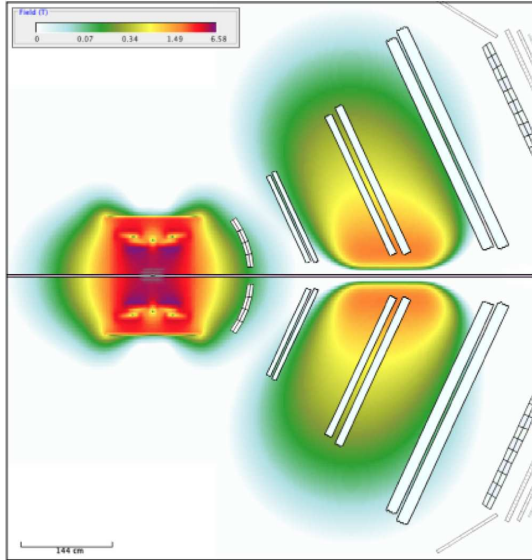


Figure 6: Combined solenoid and torus magnetic fields. The color code shows the total magnetic field of both the solenoid and torus at full current. The open boxes indicate the locations and dimensions of the active detector elements.

255 3.1. The Torus Magnet

256 A contour of one of the six identical coils of the
257 torus magnet is shown in Fig. 7. The geometri-
258 cal coverage as seen from the target ranges from 5°
259 to 40° in polar angle. The symmetrically arranged
260 six magnet coils provide an approximate toroidal
261 magnetic field around the beamline. The six coils
262 are mounted in a central cold hub on a common
263 stainless-steel cylinder, which also provides the ge-
264ometrical symmetry for the alignment of the coils
265 near the magnet center (see Fig. 8). This increases
266 placement accuracy of the coil packages in areas
267 where the magnetic field is expected to be maxi-
268 mal. A full view of the assembled torus coils and
269 cryostat is shown in Fig. 4(right). The open range
270 in azimuthal angle depends on the polar angle of
271 the particle trajectory, and ranges from 50% of 2π
272 at 5° to about 90% of 2π at 40° .

273 Each superconducting coil is made from a two-
274 coil “double-pancake” potted in an aluminum case.
275 The number of windings per pancake is 117. The
276 conductor is Superconducting Super Collider outer
277 dipole cable soldered into a 20 mm \times 2.5 mm cop-
278 per channel with a turn-to-turn insulation of 75 μm
279 fiberglass tape. Operating at a nominal current of
280 3770 A, the peak field is 3.58 T at the inner turns
281 close to the warm bore. For symmetry reasons the
282 field on the beam axis is ideally equal to zero, with
283 a small remnant field present due to imperfections
284 in the magnet assembly and coil positions. The
285 $\int B dl$ at the nominal current is 2.78 Tm at 5° and
286 0.54 Tm at 40° . The inductance of the magnet is
287 2.0 H and the stored energy 14.2 MJ. The magnet
288 has liquid-N₂ cooled heat shields. After assembly
289 and cool down, the magnet reached full field imme-
290 diately. For details on the design and operation of
291 the torus magnet, see Ref. [7].

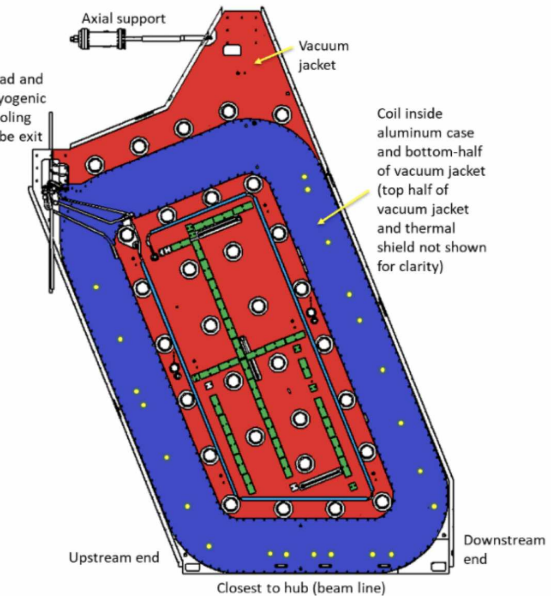


Figure 7: A torus magnet coil (blue) in its vacuum jacket. All six coils are nominally identical to each other, and are tilted forward at a 22° angle relative to the vertical, and are symmetrically arranged in azimuth. The height of the coil package is 0.3 m and the entire coil spans about 2 m \times 4 m.

292 3.2. The Solenoid Magnet

293 The solenoid magnet is a self-shielded supercon-
294 ducting magnet around the beamline used to gener-
295 ate a field primarily in the beam direction. Figure 9
296 shows the design layout of the solenoid coils, and
297 the fully assembled magnet is shown in Fig. 4(left).

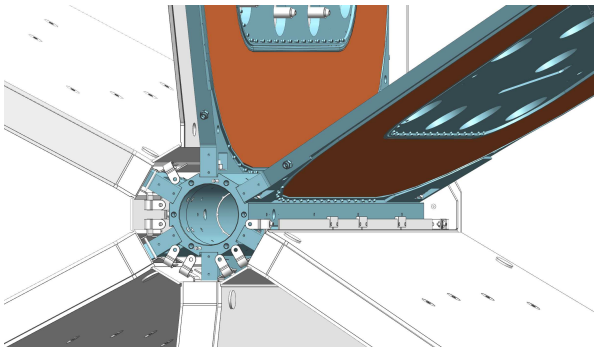


Figure 8: The six torus coils are mounted on the cold central stainless-steel hub that bears the centripetal force. The dark-shaded areas indicate the location of the superconducting coils, surrounded by the cryostat and vacuum jacket.

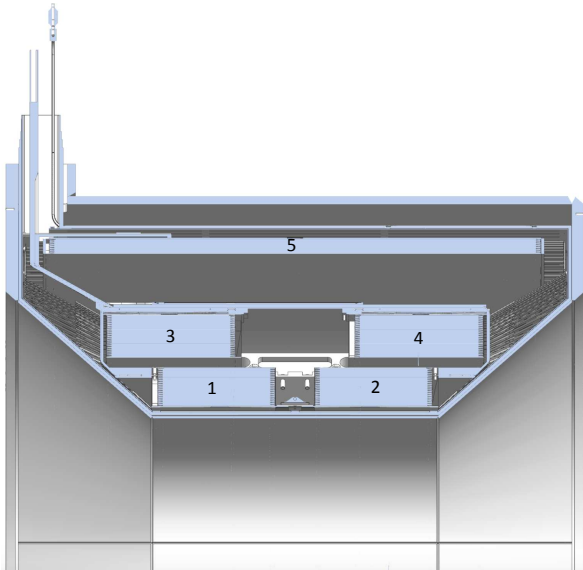


Figure 9: Cut view of the upper half of the solenoid coils with the four 2×2 main coils on the inside, and the shield coil (5) on the outside. The shield coil provides effective compensation for the magnetic field sensitive photomultiplier tubes that are located just outside of the magnet cryostat (not shown). The nominal field in the center of the magnet is 5 T.

The design is driven by the physics requirements to (a) provide a magnetic field for particle tracking at large angles, (b) act as a Møller electron shield, and (c) provide a highly uniform field at the magnet center for the operation of dynamically polarized proton and deuteron targets. Figure 10 shows the moment when the magnets had reached their full design currents. Figure 11 shows the correlation of solenoid field strength vs. current up to (and slightly beyond) the maximum current.

The magnet consists of 4 cylindrical coils arranged in two packages at different radial distances to the beamline. A fifth coil is located outside of the 4 inner coils and generates a magnetic field in the opposite direction of the field of the 4 inner coils and thus acts as an active magnetic shield. The number of turns in the main coils is 3704 ($2 \times 840 + 2 \times 1012$) and in the shield coil is 1392. The magnet is powered at a nominal current of 2416 A. At full current the solenoid generates a 5 T magnetic field at its center. The integrated field length along the magnet center is $\int B dl = 7.0$ Tm, generating a stored energy of 20 MJ. The magnet has an inner warm bore of 78 cm diameter where all of the central detectors are placed. For details on the design and operation of the solenoid magnet, see Ref. [7].

324 4. The CLAS12 Forward Detector (FD)

325 4.1. Drift Chamber (DC)

326 The six coils of the torus magnet mechanically
327 support the forward tracking system, which consists
328 of three independent DCs in each of the six sectors
329 of the torus magnet. Each of the six DC sectors
330 has a total of 36 layers with 112 sense wires,
331 arranged in 3 regions (R1, R2, and R3) of 12 layers
332 each. In each of the six torus sectors the DCs are
333 arranged identically. As displayed in Fig. 12, the R1
334 chambers are located at the entrance to the torus
335 magnetic field region, the R2 chambers are located
336 inside the magnet where the magnetic field is close
337 to its maximum, and the R3 chambers are placed
338 in a low magnetic field space just downstream of
339 the torus magnet. This arrangement provides inde-
340 pendent and redundant tracking in each of the six
341 torus sectors. Each of the 3 regions consists of 6
342 layers (called a superlayer) with wires strung at a
343 stereo angle of $+6^\circ$ with respect to the sector mid-
344 plane and 6 layers (a second superlayer) with wires
345 strung at a stereo angle of -6° with respect to the
346 sector midplane. This stereo view enables excellent
347 resolution in the most important polar angle (labo-
348 ratory scattering angle), and good resolution in the
349 less critical azimuthal scattering angle. Figure 13
350 shows the wire stringing operation for the large R3
351 chambers. For details of the DC construction and
352 performance, see Ref. [8].

353 4.2. Particle Identification

354 Cherenkov counters, time-of-flight detectors, and
355 electromagnetic calorimeters are located downstream

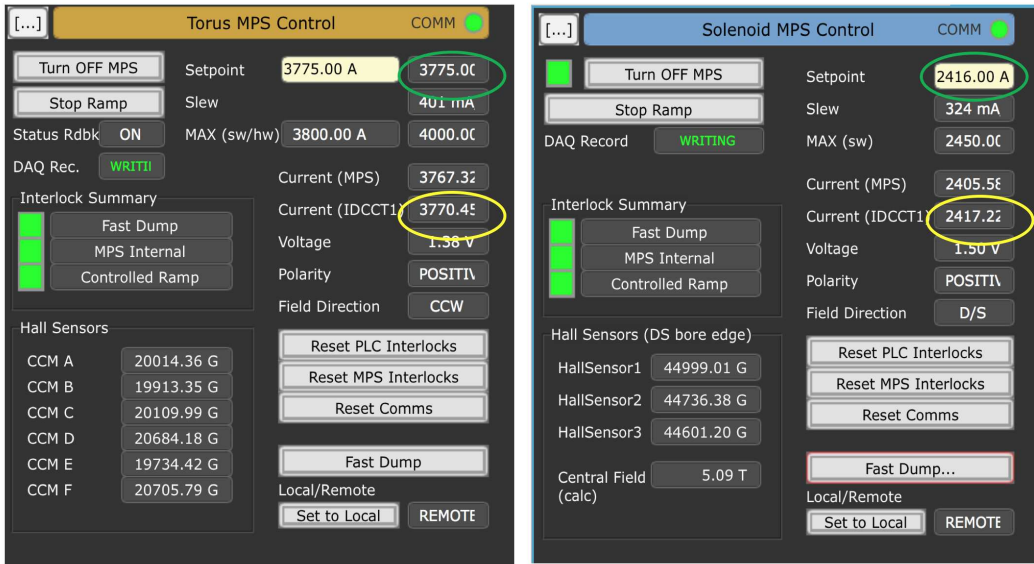


Figure 10: Energization of the torus magnet (left) and the solenoid magnet (right) to full current.

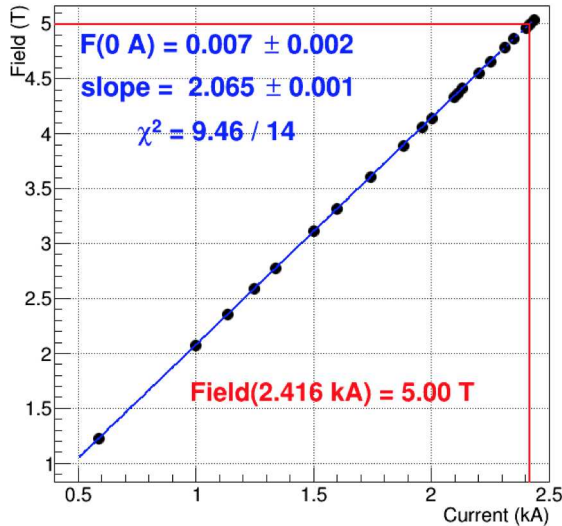


Figure 11: The excitation line of the solenoid to full current. The nominal field in the center of the solenoid magnet is 5.0 T.

of the tracking system to provide particle identification and energy measurements for electrons, high-energy photons, and neutrons. Each is described in more detail in the remainder of this section.

4.3. High Threshold Cherenkov Counter (HTCC)

The HTCC is the main detector to separate electrons (positrons) with momenta below 4.9 GeV

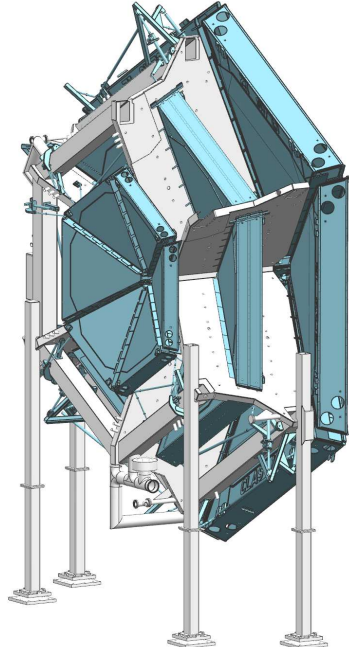


Figure 12: Drift chamber system in the CLAS12 forward tracking system from the design model. The small-size R1 chambers are located just in front of the torus magnet coils (gray shade). The medium-size R2 chambers are sandwiched between the coils of the magnet, and the large-size R3 chambers are located just downstream of the magnet.

from charged pions, kaons, and protons. The detector has full coverage of 360° in azimuth and spans



Figure 13: Simultaneous wire stringing of two R3 chambers in the Jefferson Lab clean room.

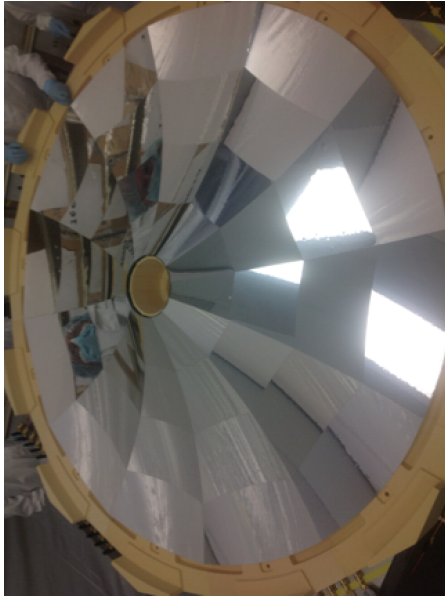


Figure 14: The HTCC mirror with its 48 mirror facets, each reflecting the Cherenkov light to a different PMT. The mirror spans a diameter of about 2.4 m.

from 5° to 35° in polar angle. It has no blind areas in its complete solid angle coverage. The detector is located downstream of the production target, sandwiched between the solenoid magnet and the torus magnet, in front of the forward tracking detectors.

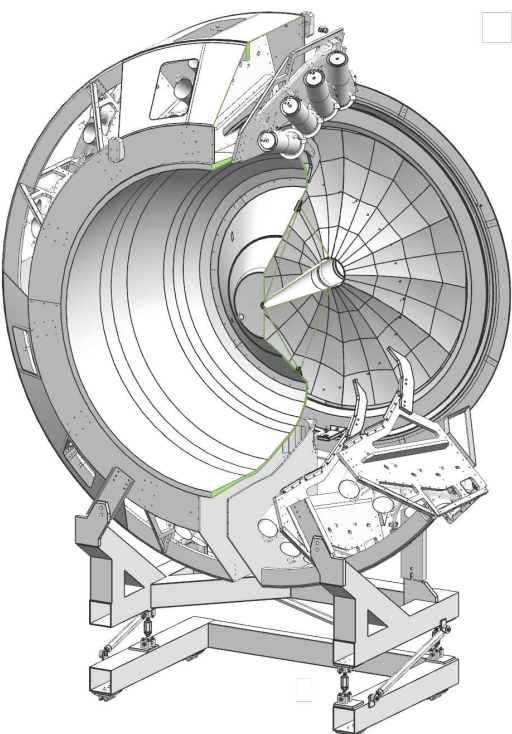


Figure 15: Cut view of the assembled HTCC detector. The container spans a diameter of about 4.5 m. The mirror is seen at the downstream end to the right. The PMTs are mounted in 12 sectors and in groups of 4 at the outer perimeter of the container. Light collection uses additional Winston cones and 5-in PMTs with quartz windows.

370 The HTCC system is required to provide high 420
 371 rejection of charged pions and low background noise 421
 372 for reliable identification of scattered electrons in 422
 373 a dense electromagnetic background environment. 423
 374 The HTCC is a single unit operated in dry CO₂ 424
 375 gas at 1 atm pressure. It is constructed using a 425
 376 multi-focal mirror of 48 elliptical mirror facets that 426
 377 focuses the Cherenkov light on 48 photomultiplier 427
 378 tubes (PMTs) with quartz windows of 125-mm 428
 379 diameter. The PMTs are located in a magnetic field 429
 380 of up to 35 G oriented along the phototube axes and 430
 381 are surrounded along their lengths by a multi-layer
 382 magnetic shield with active compensation coils.

383 In order to minimize multiple scattering in the 431
 384 HTCC detector materials and to limit its impact 432
 385 on the momentum analysis of charged tracks in the 433
 386 torus field, the HTCC mirror system is constructed 434
 387 using a backing structure of low-density composite 435
 388 material. As the detector is located in front of the 436
 389 momentum analyzing torus magnet, all materials 437
 390 but the radiator gas in the path of the charged 438
 391 particles had to be kept to a minimum. In the actual 439
 392 detector, the density of the solid material seen by 440
 393 charged particles passing through the HTCC volume 441
 394 is 135 mg/cm².

395 The HTCC is also used to generate a fast signal 442
 396 to be used as a trigger for scattered electrons. 443
 397 The HTCC operates in conjunction with energy deposited 444
 398 in the electromagnetic calorimeters to identify 445
 399 electrons of specific energies. The 360° mirror 446
 400 system of the HTCC is shown in Fig. 14. Figure 15 447
 401 shows a cut view of the assembled HTCC detector. 448
 402 For details of the HTCC construction and performance, 449
 403 see Ref. [9].

404 4.4. Low Threshold Cherenkov Counter (LTCC)

405 The LTCC system is part of the CLAS12 Forward 450
 406 Detector and is used for charged pion detection 451
 407 at momenta greater than 3.5 GeV. The LTCC 452
 408 system consists of boxes shaped like truncated pyramids. 453
 409 Four of the six sectors of CLAS12 are equipped 454
 410 with one LTCC box. Each LTCC box contains 108 455
 411 lightweight mirrors with composite backing structures, 456
 412 36 Winston light-collecting cones, 36 125- 457
 413 mm diameter PMTs, and 36 magnetic shields. The 458
 414 LTCC boxes are filled with heavy C₄F₁₀ radiator 459
 415 gas. The LTCC system has previously been used 460
 416 to detect electrons in the CLAS detector at lower 461
 417 energies [10]. It has been refurbished to provide 462
 418 higher efficiency for charged pion detection by 463
 419 increasing the volume of the radiator gas, refurbishing

420 the elliptical and hyperbolic mirrors with new coatings, 421
 421 and improving the sensitivity of the PMTs to 422
 422 Cherenkov light by coating their entrance windows 423
 423 with wavelength shifting material that absorbs 424
 424 ultraviolet (UV) light at wavelength below 300 nm 425
 425 and re-emits two back-to-back photons at larger 426
 426 wavelength. The components of the LTCC optical 427
 427 mirror system and its arrangement are shown 428
 428 in Figs. 16 and 17. For details of the LTCC 429
 429 construction, the detector refurbishment, and its 430
 430 performance, see Ref. [11].

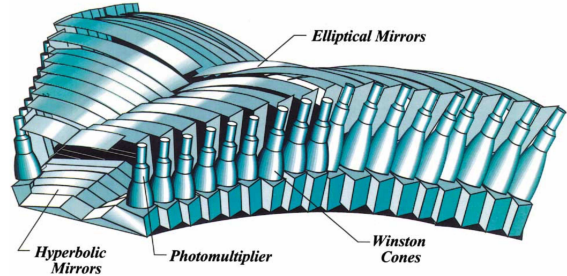


Figure 16: Layout and components of the optical mirror system within each LTCC box from the design model.

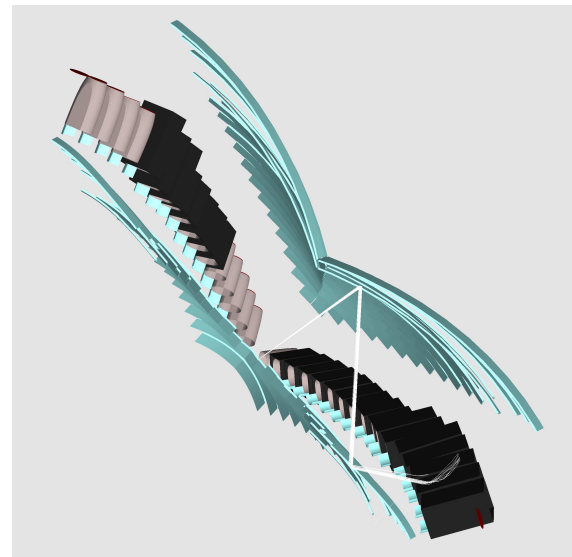


Figure 17: Perspective representation of the LTCC optical system. A charged particle enters from the bottom left and generates Cherenkov light in the radiator gas volume. The light is reflected off the elliptical mirror array towards the hyperbolic mirror array, from where it is reflected towards the Winston cone and 5-in PMT. The large acceptance coverage requires a complex mirror system for efficient light collection.

431 4.5. Ring Imaging Cherenkov Detector (RICH)

432 Some experiments require the detection and iden-
 433 tification of charged kaons in momentum ranges
 434 that are not accessible with the standard time-flight
 435 method used with the Forward Time-of-Flight sys-
 436 tem, or with the LTCC Cherenkov counters. The
 437 time-of-flight resolution of the scintillators is no longer
 438 sufficient to separate kaons from pions for momenta
 439 greater than 3 GeV. For that purpose an additional
 440 RICH detector was built and incorporated into one
 441 of the CLAS12 sectors to replace the correspond-
 442 ing LTCC sector¹. The RICH detector is designed
 443 to improve CLAS12 particle identification in the
 444 momentum range 3-8 GeV. It incorporates aerogel
 445 radiators, visible light photon detectors, and a fo-
 446 cusing mirror system that is used to reduce the
 447 detection area instrumented by photon detectors to
 448 1 m².

449 Multi-anode photomultiplier tubes (MaPMTs)
 450 provide the required spatial resolution and match
 451 the aerogel Cherenkov light spectrum in the visible
 452 and near-UV region. For forward scattered parti-
 453 cles ($\theta < 13^\circ$) with momenta 3 - 8 GeV, a proxim-
 454 ity imaging method with thin (2 cm) aerogel and direct
 455 Cherenkov light detection is used. For larger inci-
 456 dent particle angles of $13^\circ < \theta < 25^\circ$ and momenta
 457 of 3 - 6 GeV, the Cherenkov light is produced by a
 458 thicker aerogel layer of 6 cm, focused by a spherical
 459 mirror, and undergoes two further passes through
 460 the thin radiator material and a reflection from pla-
 461 nar mirrors before detection. Figure 18 shows the
 462 RICH mirror system and Fig. 19 details the optics
 463 of the detector. For further details of the RICH de-
 464 tector construction and performance see Ref. [12].

465 4.6. Forward Time-of-Flight (FTOF)

466 The FTOF system is part of the Forward De-
 467 tector and is used to measure the time-of-flight of
 468 charged particles emerging from the production tar-
 469 get during beam operation. It includes six sectors
 470 of plastic scintillators with double-sided PMT read-
 471 out. Each sector consists of three arrays of coun-
 472 ters (panel-1a - 23 counters, panel-1b 62 counters,
 473 panel-2 5 counters). The system is required for ex-
 474 cellent timing resolution for particle identification
 475 and good segmentation for flexible triggering op-
 476 tions. The detectors span a range in polar angle

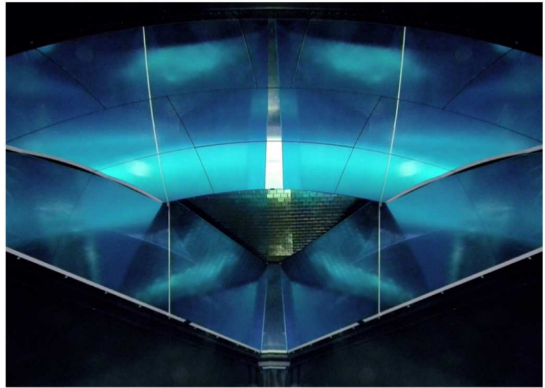


Figure 18: The RICH mirror system shown here in a per-
 spective view as seen from the entrance window, with the
 spherical mirrors above, and the planar mirrors below. The
 detector array with the MaPMTs is seen in the center. The
 aerogel radiator is not shown.

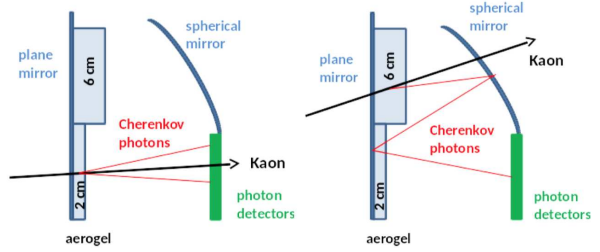


Figure 19: The principle of operation and the optics of the
 RICH detector. The left panel shows the optics for direct
 light detection and the right panel shows the optics for
 reflected light detection.

477 from 5° to 45°, covering 50% in ϕ at 5° and 90% at
 478 45°. The lengths of the counters range from 32.3 cm
 479 to 376.1 cm in panel 1a, from 17.3 cm to 407.9 cm in
 480 panel-1b, and from 371.3 cm to 426.2 cm in panel-2.
 481 The average timing resolution in panel-1a is 125 ps,
 482 85 ps in panel-1b, and 155 ps in panel-2. Figures 20
 483 and 21 show the FTOF system on the Forward Car-
 484 riage. For details of the FTOF construction and
 485 performance, see Ref. [13].

486 4.7. Electromagnetic Calorimeters (ECAL)

487 The CLAS12 detector package uses the existing
 488 electromagnetic calorimeter (EC) of the CLAS de-
 489 tector [14] and a new pre-shower calorimeter (PCAL)
 490 installed in front of the EC. Together the PCAL and
 491 EC are referred to as the ECAL. The calorimeters
 492 in CLAS12 are used primarily for the identifica-
 493 tion and kinematical reconstruction of electrons, pho-
 494 tons (e.g. from $\pi^0 \rightarrow \gamma\gamma$ and $\eta \rightarrow \gamma\gamma$ decays),
 495 and neutrons. For details of the construction of

¹A second RICH module is presently under construction and will be installed into the final CLAS12 FD sector diametrically across from the first module

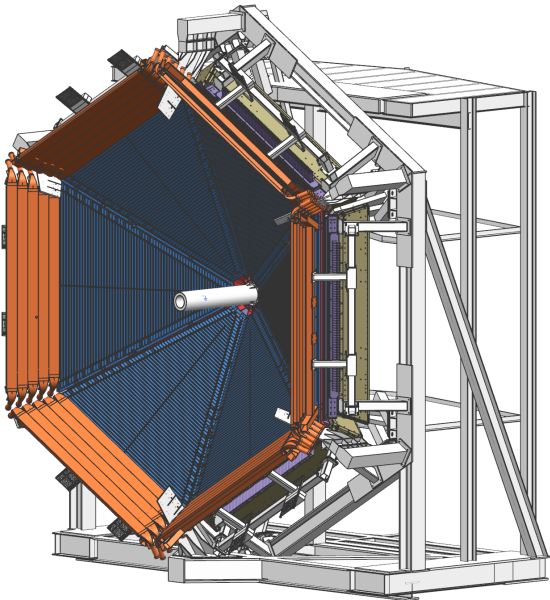


Figure 20: 3D rendering of the Forward Carriage with the FTOF system showing the panel-1b counters on the inside, and the panel-2 counters on the outside. The panel-1a counters are located immediately downstream of the panel-1b counters and are not visible here. Part of the PCAL is visible downstream of the FTOF panels.

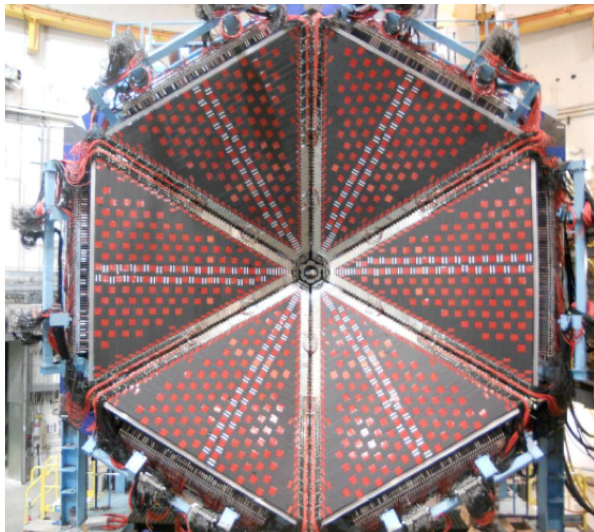


Figure 21: Photograph of the FTOF panel-1b counters mounted on the CLAS12 Forward Carriage in front of the panel-1a counters and the electromagnetic calorimeters before the installation of the panel-2 counters.

the PCAL and the performance of the ECAL, see Ref. [15].

The PCAL and EC are both sampling calorimeters consisting of six modules. Along the direc-

tion from the target, the EC consists of two parts, read out separately, called EC-inner and EC-outer. They provide longitudinal sampling of electromagnetic showers, as well as of hadronic interactions to improve particle identification. Each module has a triangular shape with 54 (15/15/24, PCAL/EC-inner/EC-outer) layers of 1-cm-thick scintillators segmented into 4.5/10-cm (PCAL/EC) wide strips sandwiched between 2.2-mm-thick lead sheets. The total thickness corresponds to approximately 20.5 radiation lengths. Scintillator layers are grouped into three readout views with 5/5/8 PCAL/EC-inner/EC-outer layers per view, providing spatial resolutions of less than 2 cm for energy clusters. The light from each scintillator readout group is routed to the PMTs via flexible optical fibers. Figure 22 shows the PCAL after installation on the Forward Carriage in front of the existing EC from CLAS.

4.8. Forward Tagger (FT)

The Forward Tagger (FT) extends the capabilities of CLAS12 to detect electrons and photons at very forward polar angles in the range from $2.5^\circ \leq \theta \leq 4.5^\circ$. The detection of forward-going scattered electrons allows for electroproduction experiments at very low photon virtuality Q^2 , providing an energy-tagged, linearly polarized, high-intensity, quasi-real photon beam. This configuration enables execution of an extensive hadron spectroscopy program. The FT consists of a calorimeter, a micro-strip gas tracker, and a hodoscope. The electromagnetic calorimeter with 332 lead-tungstate (PbWO_4) crystals is used to identify electrons, measure the electromagnetic shower energy, and provide a fast trigger signal. The tracking system in front of the calorimeter measures the charged particle scattering angles, and the scintillator hodoscope aids in separating electrons and high-energy photons.

Figure 23 shows a photograph of the FT during cosmic ray studies before its installation in CLAS12. During beam operations, a tungsten shielding pipe of conical shape is installed in front of the FT to absorb Møller electrons and low-energy photons produced by beam interactions with the target and downstream materials. This shield protects both the FT and the Forward Detectors from electromagnetic background. The cone angle is 2.5° , compatible with the FT acceptance. In this configuration, known as “FT-ON”, the FT can be used to detect both electrons and photons, extending the detection capabilities of CLAS12 . Alternatively, when

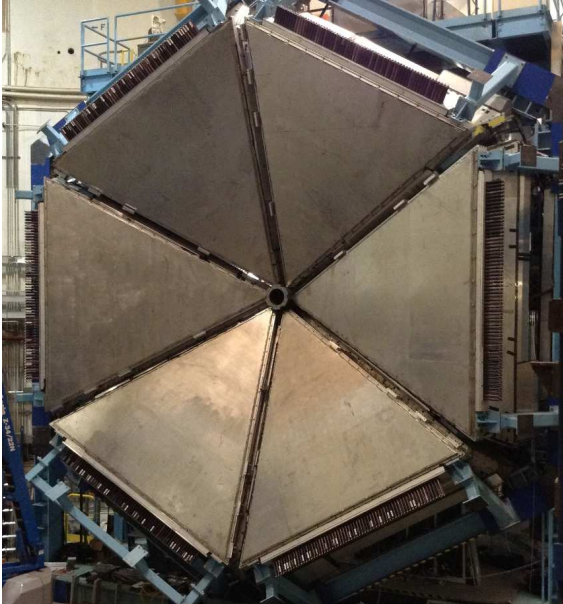


Figure 22: PCAL after installation on the Forward Carriage in front of the existing EC.

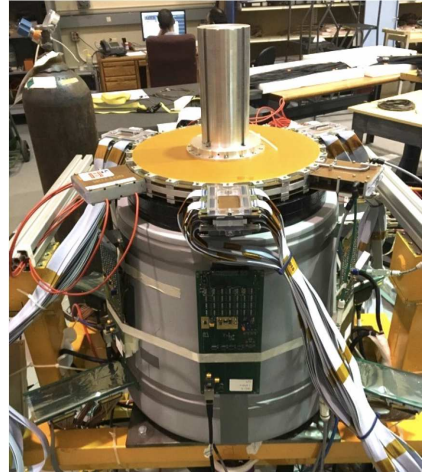


Figure 23: The Forward Tagger system during cosmic ray testing before installation in CLAS12. The lower part contains the electromagnetic calorimeter composed of lead-tungstate crystals. The upper part includes the hodoscope and the tracking disks. Here the FT is rotated by 90° compared to its installation configuration.

the FT is not needed for the physics program, the FT detectors are turned off and additional shielding elements are installed in front of the FT covering up to 4.5° to reduce the background in the DC R1 chambers. This configuration, known as “FT-Off”, reduces the accidental background by one-third at the same beam conditions, which allows for higher luminosity data taking with CLAS12. Further details on the FT are described in Ref. [16]. Figure 24 shows a rendering of the FT setup near the entrance to the warm bore of the torus magnet.

5. The CLAS12 Central Detector (CD)

Particles scattered from the target at polar angles in the range from 35° to 125° are detected in the Central Detector with its own particle identification and tracking detectors. Charged particles are tracked in the Central Vertex Tracker (CVT) and detected in the Central Time-of-Flight (CTOF) detector with full 360° coverage in azimuthal angle. Neutron detection is provided by the Central Neutron Detector (CND) located radially outside of the CVT and the CTOF. The fully assembled CD is shown in Fig. 25 after installation in the solenoid. Figure 26 shows the Central Detector from the upstream end.

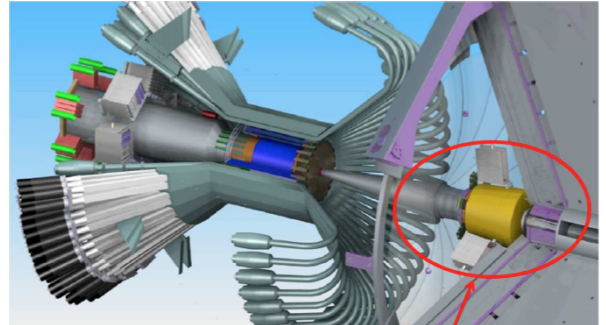


Figure 24: The Forward Tagger system (circled) downstream of the Central Detector in front of the torus magnet warm bore entrance.

5.1. Central Vertex Tracker (CVT)

The CLAS12 CVT is a part of the Central Detector and is used to measure the momentum and to determine the vertex of charged particles scattered from the production target, which is centered within the solenoid magnet. Details of the tracking system are shown in Fig. 27. It consists of two separate detectors, a Silicon Vertex Tracker (SVT) and a Barrel Micromegas Tracker (BMT). The SVT system includes 3 regions with 10, 14, and 18 double-sided modules of silicon sensors instrumented with the digital readout ASIC Fermilab Silicon Strip Readout (FSSR2). The readout pitch is 156 μm, and the total number of channels

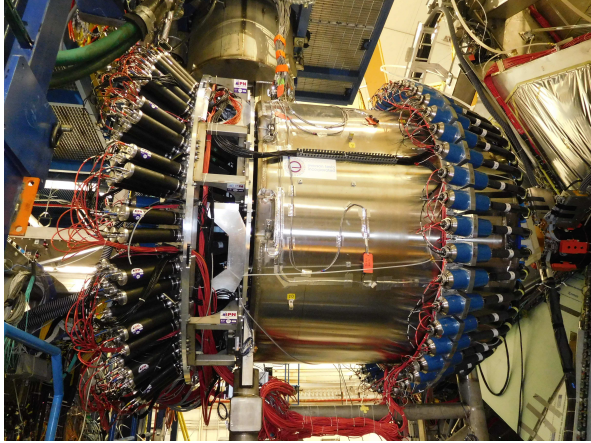


Figure 25: The Central Detector installed in the solenoid magnet in a side view. The readout PMTs are seen at the upstream end (left) and at the downstream end (right) of the solenoid.

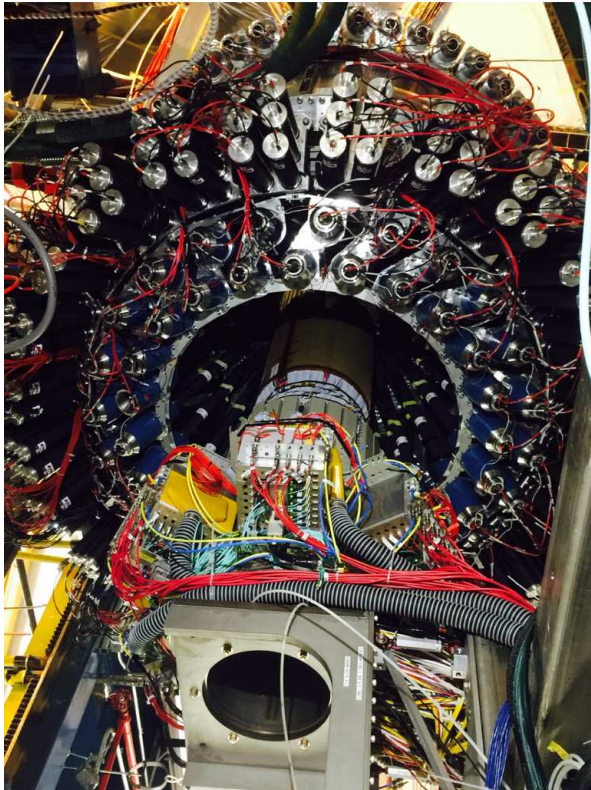


Figure 26: The Central Detector seen from the upstream end. The central tracker system is shown in a retracted position for maintenance. During operation it is fully inserted into the warm bore of the magnet.

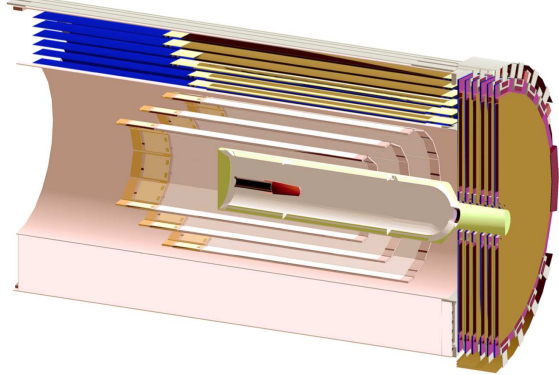


Figure 27: Central Vertex Tracker schematic, showing (from the inside) the target cell and vacuum chamber, the 3 double layers of the SVT, followed by the 6 layers of the BMT. The beam enters from the left. The six FMT layers are shown at the downstream end at the right.

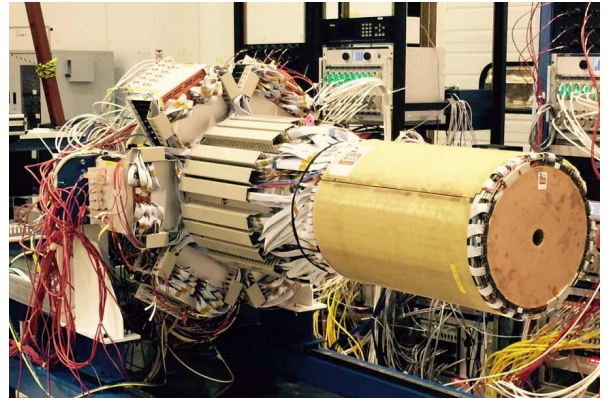


Figure 28: The fully assembled Central Vertex Tracker with the SVT, BMT, and FMT. The BMT and FMT are shown on the outside. The FMT has a circular opening in the center for the electron beam to pass through. The SVT is encapsulated and hidden from view.

590 is 21,504. See Ref. [17] for details on the design,
591 construction, and performance of the SVT.

592 The BMT contains 3 layers of strips along the
593 beamline and 3 layers of circular readout strips around
594 the beamline, with a total number of 15,000 read-
595 out elements. The BMT provides important im-
596 provements in momentum resolution and in track-
597 ing efficiency. Each layer is arranged azimuthally in
598 3 segments of 120° azimuthal coverage each. The
599 system operates at the full design luminosity of
600 $10^{35} \text{ cm}^{-2}\text{s}^{-1}$.

601 Another component of the CVT is the Forward
602 Micromegas Tracker (FMT), consisting of 6 lay-

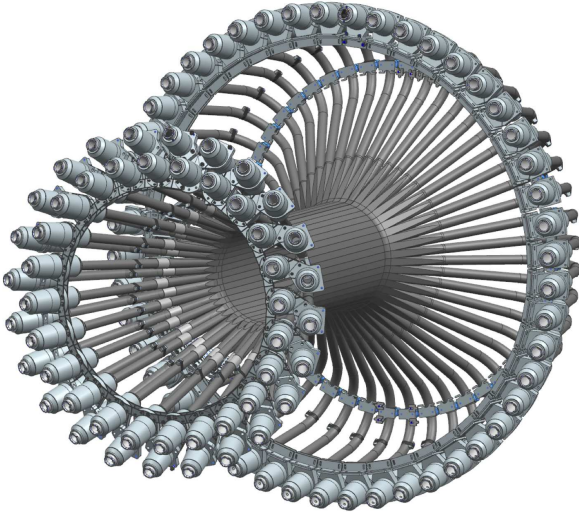


Figure 29: The CTOF detector with its 48 scintillator bars outfitted with light guides, PMTs, and magnetic shields at both ends of each counter.

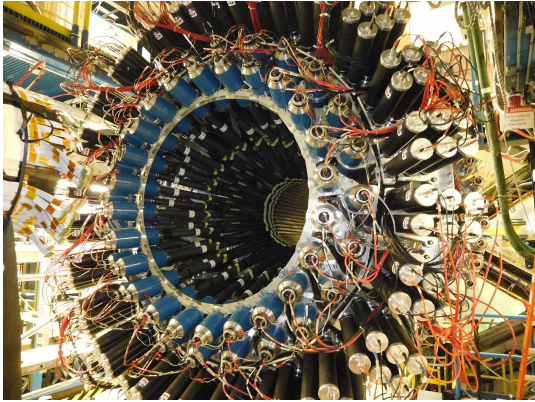


Figure 30: The fully assembled CD as seen from its upstream end with the 144 CND light guides and PMTs at the three outermost rings, and the 48 PMTs of the CTOF (two inner rings).

ers with 6,000 readout elements. It is integrated mechanically with the CVT to provide a compact tracking system, but covers the polar angle range from 5° to 35° and provides improved vertex reconstruction for forward-scattered charged particles. The fully assembled CVT, including the FMT, are shown in Fig. 28. See Ref. [18] for details on the BMT and on the FMT.²

²The FMT was not used during the experimental runs covered in this paper.

611 5.2. Central Time-of-Flight (CTOF)

612 The CTOF system is used for the identification
 613 of charged particles emerging from the target
 614 via time-of-flight measurements in the momentum
 615 range from 0.3 to ~ 1.25 GeV. The CTOF includes
 616 48 plastic scintillators with double-sided PMT read-
 617 out via, respectively, 1.0-m-long upstream and 1.6-
 618 m-long downstream focusing light guides. The ar-
 619 ray of counters forms a hermetic barrel around the
 620 target and the CVT. The barrel is aligned with the
 621 beam axis inside the 5 T solenoid magnet. The
 622 PMTs are placed in a region of 0.1 T fringe field
 623 of the solenoid and enclosed within a triple layer
 624 dynamical magnetic shield [19] that provides less
 625 than 0.2 G internal field near the PMT photocathode.
 626 The CTOF system is designed to provide time
 627 resolution of 80 ps for charged particle identifica-
 628 tion in the CLAS12 Central Detector. Details of
 629 the CTOF are described in Ref. [20]. Figure 29
 630 shows the CTOF system from the design model and
 631 Fig. 30 shows the upstream end of the CTOF in-
 632 stalled inside the solenoid.

633 5.3. Central Neutron Detector (CND)

634 The CLAS12 CD is also equipped with the CND
 635 positioned radially outward of the CTOF that al-
 636 lows the detection of neutrons in the momentum
 637 range from 0.2 to 1.0 GeV by measurement of their
 638 time-of-flight from the target and the energy de-
 639 position in the scintillator layers. The detector is
 640 made of three layers of scintillator paddles (48 pad-
 641 ples per layer), coupled two-by-two at the down-
 642 stream end with semi-circular light guides and read
 643 out at the upstream end by PMTs placed outside of
 644 the high magnetic field region of the solenoid. The
 645 scintillators are connected to 1-m-long bent light
 646 guides. Figure 30 shows the upstream readout end
 647 of the CND installed in the solenoid. Details of the
 648 CND are described in Ref. [21].

649 5.4. Back Angle Neutron Detector (BAND)

650 Neutron detection at back angles is accomplished
 651 with the BAND, which is positioned 3 m upstream
 652 of the CLAS12 target to detect backward neutrons
 653 with momenta between 0.25 and 0.7 GeV. It con-
 654 sists of 18 horizontal rows and 5 layers of scintillator
 655 bars with PMT readout on each end to measure
 656 time-of-flight from the target. There is an addi-
 657 tional 1-cm scintillation layer for vetoing charged
 658 particles. The detector covers a polar angle range
 659 from 155° to 175° with a design neutron detection

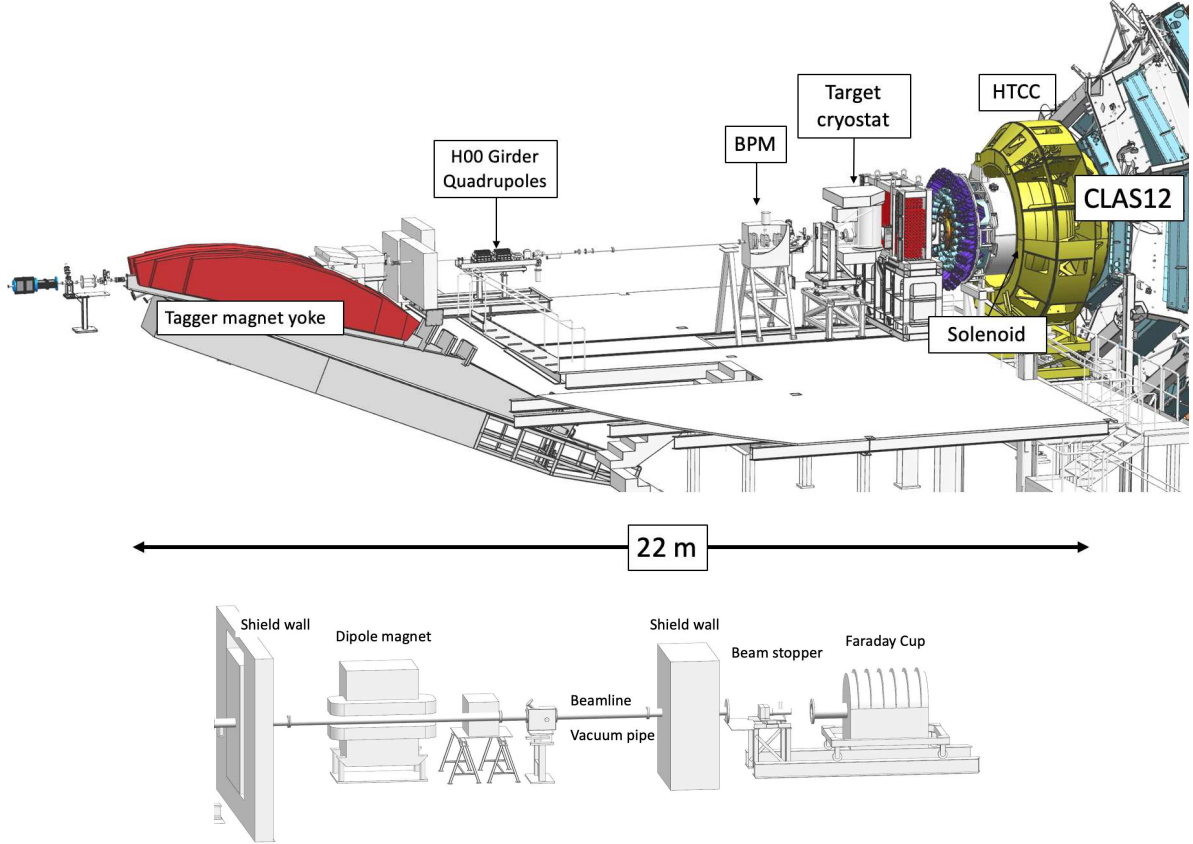


Figure 31: Top: Hall B beamline upstream of the target, showing the tagger magnet (red) to the left, which is energized during beam tuning and during polarization measurements. The doublet seen downstream of the tagger is a pair of quadrupoles. The beam position monitors (BPMs) are used for beam position and beam current measurements. The main element on the right is the solenoid magnet nearly fully encapsulated by the HTCC (yellow). Several of the torus magnet coils are visible at the far right. Bottom: The part of the beamline that extends from the downstream end of CLAS12 to the Faraday cup, a total absorbing device that is used to integrate the beam current to get the total accumulated charge.

efficiency of 35% and a momentum resolution of about 1.5%. Details will be provided in Ref. [22].

6. Hall B Beamline

The Hall B beamline has two sections, the 2C line, from the beam switch yard (BSY) to the Hall proper, and the 2H line, from the upstream end of the experimental Hall to the beam dump (or Faraday cup) in the downstream tunnel. Figure 31 shows the portion of the 2H line from the tagger dump magnet to the entrance to CLAS12 and the portion of the 2H line downstream of CLAS12 leading to the Faraday cup.

The beamline instrumentation consists of beam optics, beam position and beam current monitors,

beam viewers, collimators, shielding, beam profile scanners, and beam halo monitors. Devices that control the beam direction, its profile, and measure critical parameters, are under the accelerator operations control. Hall B operators control collimators, halo monitors, profile scanners, and viewers. They are also responsible for configuration and running the Møller polarimeter located upstream of the tagger magnet.

The tagger magnet on the left of Fig. 31 (in red) is not energized during production data taking. When energized the yoke of this magnet serves as a beam dump that is used during beam tuning before the beam is directed on the Hall B production target. It is also used during specialized runs, such as polarization measurements in the upstream beam-

line, to avoid exposure of sensitive CLAS12 detectors to high background loads. For details of the beamline elements and beam quality, see Ref. [23].

The performance of the electron beam and all diagnostic elements in the beamline, status of the beamline vacuum, the superconducting magnets, and the rates in all detector systems that are indicative of potential beam quality issues are directly displayed on a single master screen that is accessible to the shift personnel and other experiment-related personnel and experts. Figure 32 shows the details of the monitoring screen.

6.1. Monte Carlo Simulations

A critical part of operating an open large-acceptance detector system at high luminosities is the simulation not only of hadronic events but also, and more importantly, the simulation of the beam-related accidental hits in the tracking systems. The source of accidentals is primarily from the beam electron elastically scattering off atomic electrons (Møller electrons) and their secondary interaction with beamline components. The production rate is orders of magnitude larger than the hadronic production rate. These background sources have to be shielded through careful design of magnetic channeling, as well as a proper design and careful optimization of the beamline shielding and the vacuum pipe to minimize interaction of these electrons with high- Z material. The availability of a realistic simulation package was essential for the optimal design of the CLAS12 integrated detector concept.

The strong solenoid field is essential in channeling the scattered Møller electrons through the beam enclosure to avoid interactions with the beamline materials. Figure 33 shows a single randomly triggered event at 50% of full luminosity in a time window of 250 ns. This corresponds to the time window in the R1 drift chambers used in the event reconstruction. The main conclusion is that only when both magnets are energized can the detector be operated with acceptable background levels (see Fig. 33 lower left). Additionally, a realistic simulation package is essential for the normalization of cross sections, especially to take into account the detector occupancies for data taking at luminosities near or above the maximum design luminosity where the track reconstruction efficiency can be significantly affected by accidentals. In order to quantitatively account for this, data were taken at different beam currents (i.e. different luminosities) with randomly triggered events. Data from these

randomly triggered events were merged with simulated physics events to study the loss of real tracks for different data runs. See Ref. [24] for details on the CLAS12 Geant4 simulation package GEMC.

6.2. Experimental Targets

Hall B experiments are grouped into running periods with similar beam energy, detector configuration, magnet settings, and target material. The most common target materials have been liquid hydrogen and liquid deuterium. Other materials include solid nuclear targets of various kinds from ^{12}C to ^{208}Pb , depending on the physics requirements. For some specialized experiments high-pressure gas targets are used. All targets are positioned inside CLAS12 using support structures that are inserted from the upstream end, and are independent of the detector itself.

A large science program with CLAS12 requires the use of spin-polarized protons and neutrons. Spin-polarized protons and polarized neutrons are used in compound materials where the hydrogen or deuterium can be spin polarized using microwave-induced electron spin transitions in molecules such as in NH_3 and ND_3 . Certain electron spin-flips can be transferred to the proton or neutron in the hydrogen or deuterium atoms, and lead to high polarization of up to 90% for the free protons and over 50% in neutrons of the deuterium atoms in this process of dynamical polarization. To achieve high levels of polarization, a high magnetic field of 5 T is required. In CLAS12, the required magnetic field is externally provided by the 5 T field in the center of the solenoid magnet, which has been designed to provide a homogeneous magnetic field of $\Delta B/B_0 \leq 10^{-3}$ within a cylindrical region of diameter $\phi = 2.5$ cm and $\Delta z = 4$ cm along the beamline. The region near the target cell includes additional correction coils to achieve a factor of 10 better homogeneity that is needed for polarizing the deuterium nuclei in ND_3 . Other polarized materials, such as polarized HD (called HD-Ice), will also be used in support of programs that require spin-polarized targets with the polarization axis oriented transverse to the direction of the electron beam.

7. Data Acquisition and Trigger System

7.1. CLAS12 Data Flow and Monitoring

During data taking the quality of the data is continuously monitored by displaying a very small

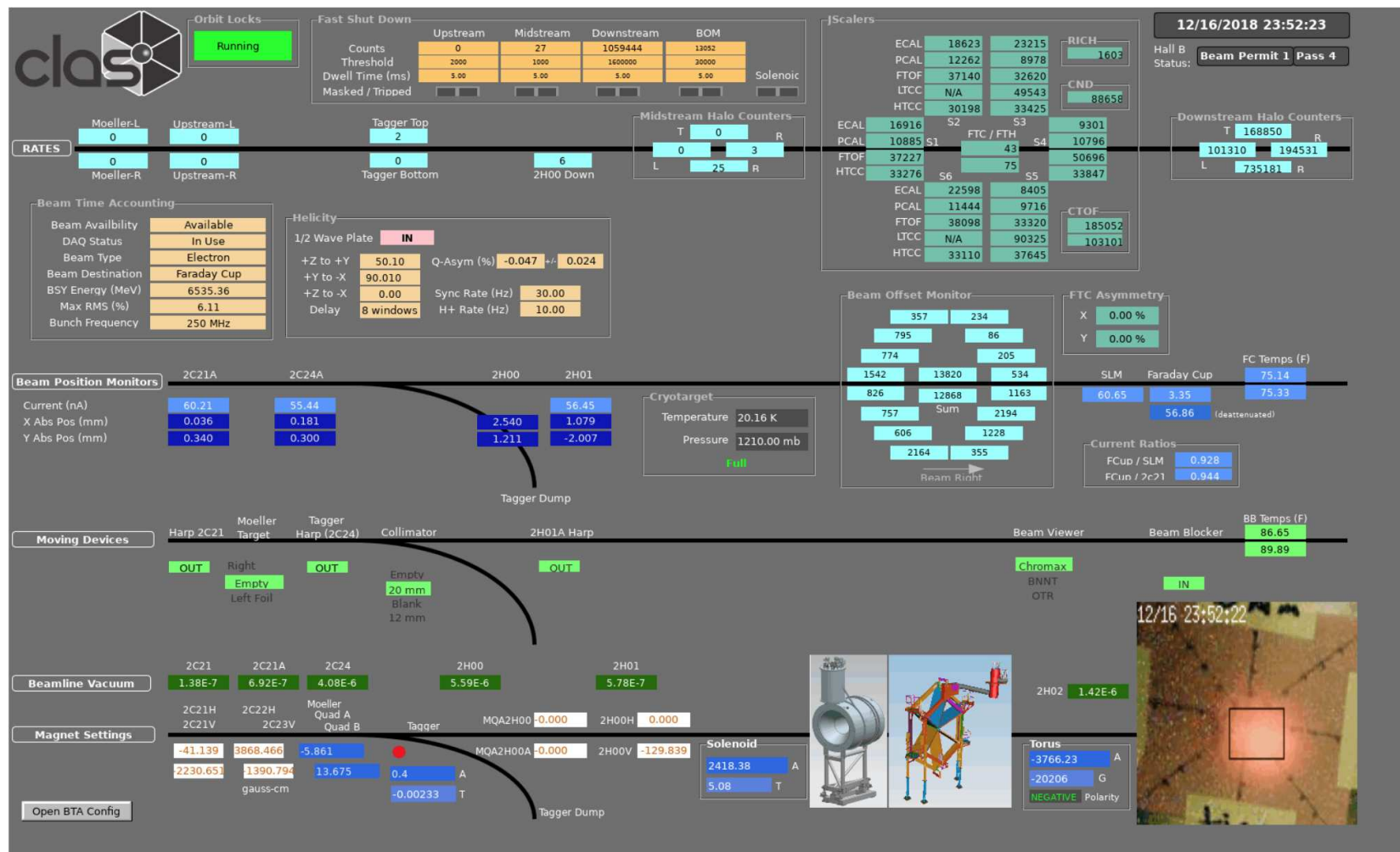


Figure 32: The CLAS12 beamline and detector monitoring systems in Hall B. Top line (left to right) shows the beam halo counters (that typically have zero or single digit rates if the beam quality is good), detector integrated rates in all six sectors, and halo counter rates downstream of the target. Second line: beam position and beam current monitors, status of the cryogenic target, beam offset monitor (16 counters around the beam just upstream of the target), and Faraday cup information. Third line: Devices that can be moved in and out of the beam used for beam viewing and profile measurements, and polarization measurements with Möller scattering. Fourth line: Beamline vacuum conditions, beamline quadrupole settings, CLAS12 torus and solenoid settings, Chromax beam viewer, and beam blocker in front of the Faraday cup.

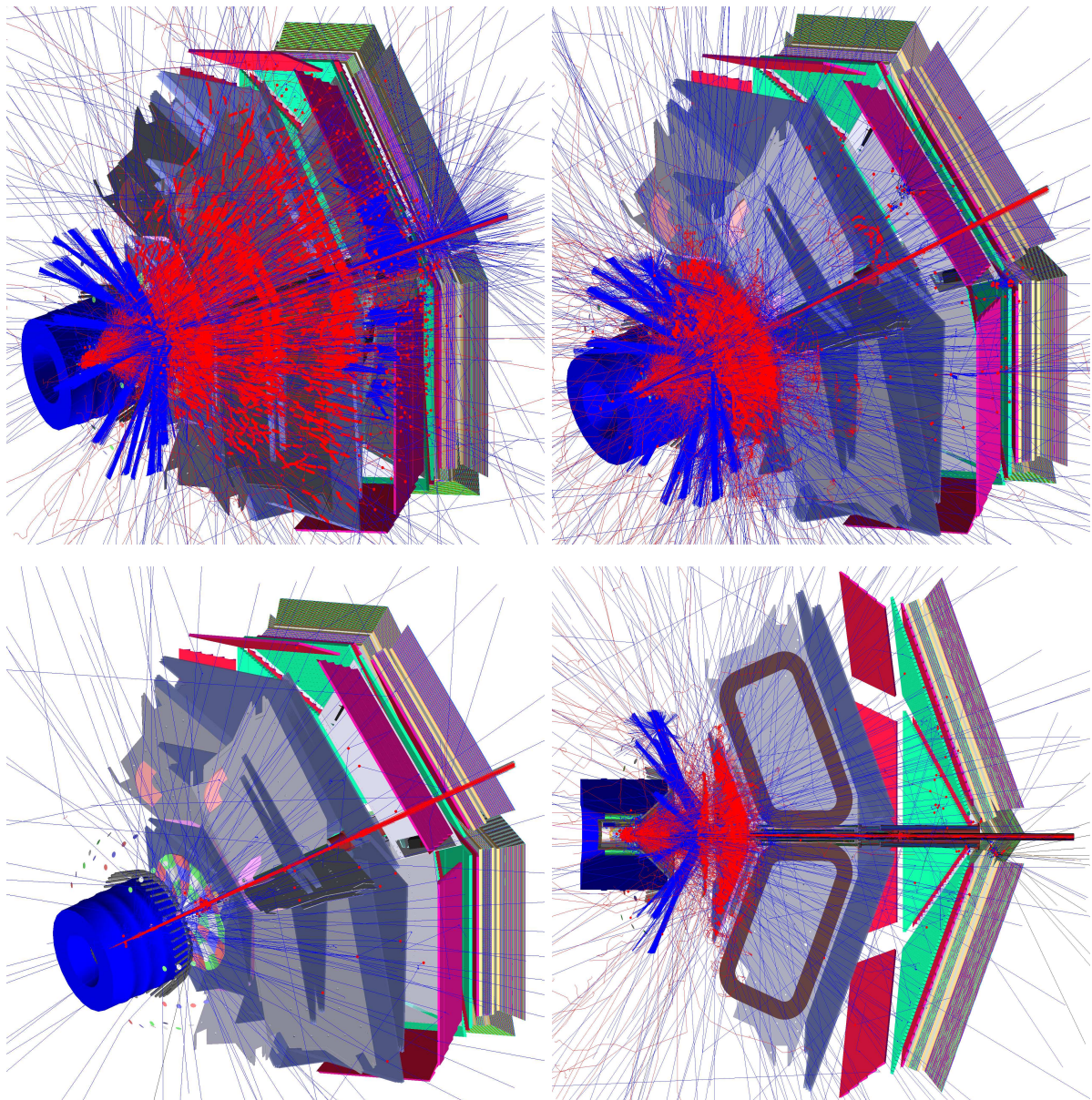


Figure 33: Geant4 representations of accidental background events occurring within a 250 ns time window at different magnetic field configurations and at 50% of design luminosity. Top left: Solenoid field is OFF and torus field is OFF. Top right: Solenoid field is OFF and torus field is ON. Bottom right: Rotated 2D view of top right. Bottom left: Solenoid field is ON and torus field is ON. Color code: red lines are primary electrons; red circles are hits in the detectors; blue lines are photons, including the Cherenkov light, which is clearly visible as the narrow light bundles just at the downstream end of the solenoid magnet, created by the Møller electrons in the HTCC when the solenoid magnet is OFF.

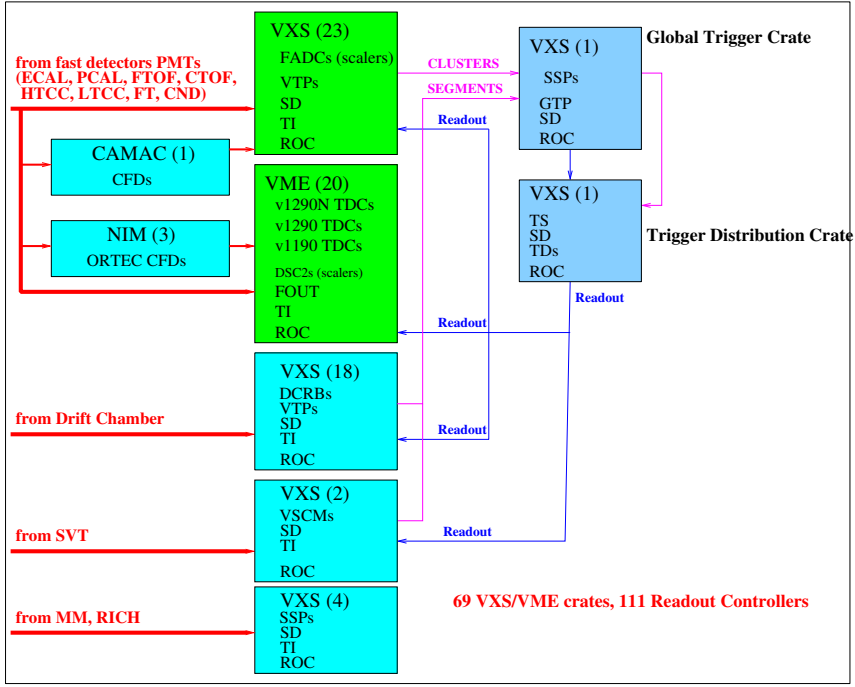


Figure 34: Schematic diagram of the CLAS12 data acquisition and trigger system.

fraction of single events in the CLAS12 event display (*ced*) that allows immediate action by the shift personnel in case of any malfunctioning detector elements or electronics modules. Monitoring histograms are also filled on a regular basis that include detector subsystem channel occupancies, as well as simple analysis plots and can be easily compared with results collected earlier during the data taking.

The CLAS12 data acquisition (DAQ) system is designed for an average of 20 kHz Level 1 (L1) trigger rate, pipelined for continuous operation. The sector-based L1 triggers support data streaming, subsystem hit patterns, and energy summing with low threshold suppression. The scalable trigger distribution scheme uses 111 front-end L1 crates. CLAS12 uses different programmable features for each detector that participates in the L1 trigger. A schematic diagram showing a complete overview of the DAQ system is shown in Fig. 34. In 2018 the DAQ was run at trigger rates of typically 15 kHz and data rates of up to 500 MB/s with a livetime of >95%. At somewhat lower livetime of ~90%, trigger rates of 20 kHz and data rates of up to 1 GB/s have been achieved. Details of the design, functionality, and performance of the CLAS12 DAQ are provided in Ref. [25].

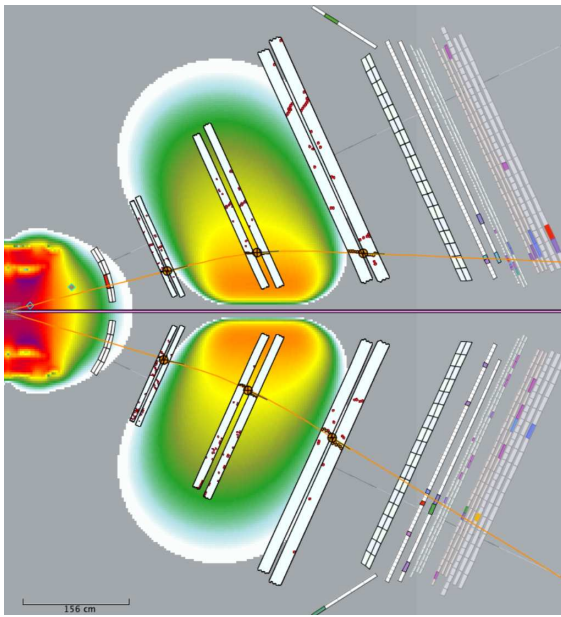
7.2. Fast and Selective Triggers

CLAS12 uses a series of fast triggers that are tailored to a specific event pattern selection. Most of the physics experiments require the electron scattered on the production target to be detected as it defines the mass (Q^2) and kinematics of the virtual photon as $Q^2 = -(e - e')^2$, where e and e' are the 4-momentum vectors of the beam electron and of the scattered electron, respectively. The scattered electron is uniquely identified with signals in the HTCC and clustered energy deposition in the ECAL.

At the nominal design luminosity of CLAS12, the hadronic production rate is approximately 5×10^6 /s. However, only a small fraction of the events is of interest for the science program with CLAS12. In particular, most physics reactions require the detection of the scattered electrons at some finite scattering angle, for example $\theta_{e'} > 5^\circ$. Figure 35 shows one example of an electron-triggered event with one additional positively charged track. The trigger purity depends on the polarity of the torus magnet and on the beam-target luminosity. Only about 50% of the electron triggers recorded with an inbending torus polarity are actually electrons. For the outbending torus polarity, the electron trigger purity is as high as 70%. In trigger definition list, charged particles in either the FD or the CD

843 can also be selected in the trigger in addition to
 844 the scattered electron making use of the detector
 845 responses.

846 In some experiments the detection of electrons
 847 in the FT is of interest if they are associated with
 848 hadronic event patterns of one or two additional
 849 detected hadrons. Such conditions have been im-
 850 plemented in the fast trigger decision that reduces
 851 the number of triggers to about 2×10^4 events/s, i.e.
 852 by a factor of 250 from the hadronic rate. The data
 853 rate is typically 500 MB/s under such conditions
 854 and can be handled by the CLAS12 data acquisi-
 855 tion system and the available computing resources.
 856 Figure 36 shows an example of specific triggers con-
 857 figurations that have been used during the fall 2018
 858 run period. Details of the design, functionality, and
 859 performance of the CLAS12 trigger system are pro-
 860 vided in Ref. [26].



861 Figure 35: View of an event in CLAS12 from the *ced* event
 862 display. Predefined trajectories from a look-up table are em-
 863 ployed to select hit patterns in the 3 DC regions that
 864 correspond with localized energy deposition in the ECAL.
 865 For the two-track trigger, the two sectors show DC hit pat-
 866 terns for tracks with opposite charges. The upper track is an
 867 electron, shown by the hit in the HTCC that bends towards
 868 the beamline. The lower track has positive charge and bends
 869 away from the beamline.

8. CLAS12 Offline Software

882 The CLAS12 offline event reconstruction is de-
 883 signed to analyze large amounts of beam-induced



862 Figure 36: The CLAS12 trigger control screen during a spe-
 863 cific data run with a total of 17 active triggers operating
 864 at a livetime of 95.4%. Nearly half (48.7%) of all triggers
 865 are from single electrons detected in one of the 6 FD sectors.
 866 Over a quarter (27.81%) of all triggers required an electron in
 867 the FT with an additional two charged hits detected in the
 868 FTOF and in the PCAL. Several others were taking data
 869 at the 5% level and required charged tracks in the FTOF
 870 and ECAL in opposite FD sectors. Finally, several other
 871 triggers were used for monitoring purposes and were heavily
 872 pre-scaled.

864 experimental data acquired during production and
 865 cosmic ray runs; the latter being used for alignment
 866 and calibration purposes. The CLAS12 reconstruc-
 867 tion framework is built based on a service-oriented
 868 software architecture, where the reconstruction of
 869 events is separated into micro-services that execute
 870 data processing algorithms. The software packages
 871 consist of the event reconstruction, visualization,
 872 and calibration monitoring services, as well as de-
 873 tector and event simulations.

874 During the CLAS12 design phase a realistic sim-
 875 ulation package based on Geant4 was developed to
 876 aid in the optimization of the detector hardware re-
 877 sponse to beam interactions in terms of resolution,
 878 robustness of operation at high luminosity, details
 879 of the beamline design, and other aspects.

8.1. Event Reconstruction

880 Event reconstruction in the CLAS12 FD con-
 881 sists of the identification of charged and neutral

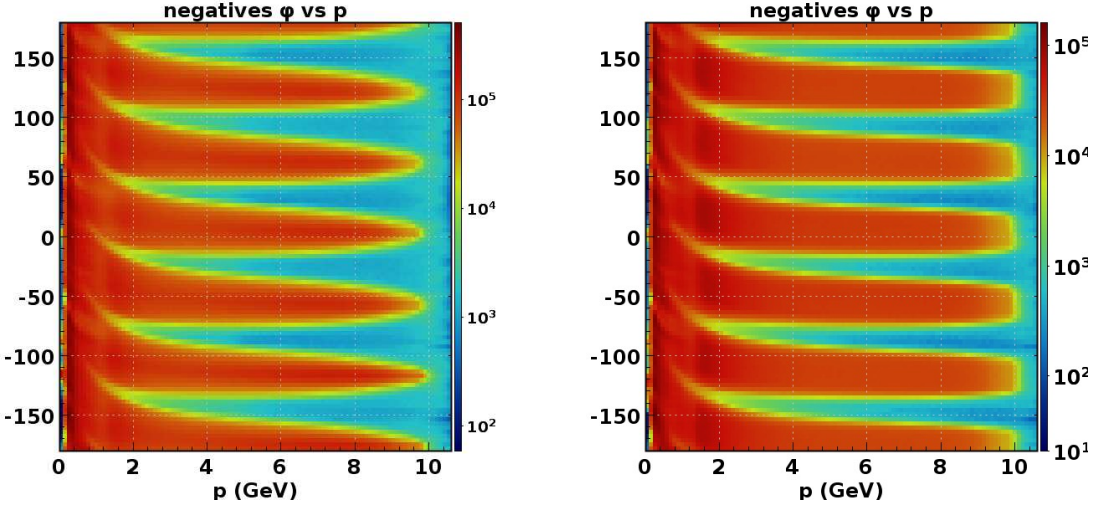


Figure 37: Particle distributions in azimuthal angle (ϕ) vs. momentum in the CLAS12 FD for inbending electrons (left) and with reversed torus field for outbending electrons (right) at a beam energy of 10.6 GeV. The azimuthal angle is measured at the production vertex. The azimuthal distribution of inbending electrons narrows with increasing momentum, as high-momentum electrons in CLAS12 are bent towards the beamline, where detector acceptances are reduced. This is not the case for outbending electrons that are deflected away from the beamline toward larger detector acceptances. The $p - \phi$ correlation, most visible at low momentum, is due to the solenoidal magnetic field that bends charged tracks dependent on their transverse momentum component and on their charge. For positively charged tracks the ϕ motion is in the opposite direction from negative (electron) tracks. Color axes indicate the particle yields.

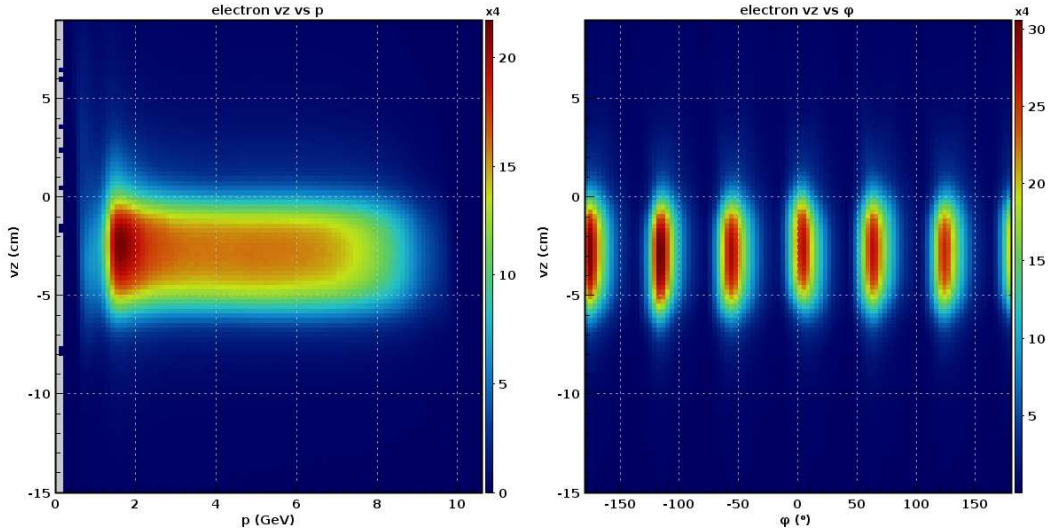


Figure 38: Reconstructed vertex along the beamline v_z for electrons in the FD. Left: v_z vs. momentum, Right: v_z vs. azimuthal angle. The vertical size of the vertex band is consistent with the target length of 5.0 cm.

883 particles along with the determination of their 3- 889
 884 momenta and reaction vertex at the distance of 890
 885 closest approach to the beamline. Charged particle 891
 886 reconstruction requires both forward tracking and 892
 887 FTOF information. 893

888 Track reconstruction in the FD is based on a hit 894

clustering algorithm that requires at least 4 out of 6 connected DC cells to form a track segment within each superlayer. The tracking algorithm requires at least 5 out of 6 superlayers in a sector to form a track candidate. The first stage of tracking relies solely on the DC wire positions to fit the tracks and

895 to provide matching to the outer detectors subse- 947
 896 quently required to obtain timing information. At 948
 897 the second stage of tracking, timing information is 949
 898 used to determine a time-based track and the par- 950
 899 ticle momentum and flight path, while the FTOF 951
 900 gives the particle velocity (β) when combined with 952
 901 flight-path information (see Ref. [27] for details). 953
 902 The momentum and velocity information are com- 954
 903 bined to give the particle mass: $m = p/\beta\gamma$. Elec- 955
 904 tron identification additionally requires the track 956
 905 to match in time and position with both an HTCC 957
 906 hit and an isolated shower in the ECAL. The en- 958
 907 ergy of the shower must be consistent with the track 959
 908 momentum measured by the DCs in the torus mag- 960
 909 netic field. 961

910 Charged particles are tracked in each sector sep- 962
 911 arately using the 3 regions of DCs in each sec- 963
 912 tor. Most tracks are confined within one sector as 964
 913 the magnet optics and the massive mechanical sup- 965
 914 port of the torus coils prevent most tracks from 966
 915 crossing from one sector into a neighboring sec- 967
 916 tor. In rare cases low-momentum charged pions 968
 917 can cross from one sector into the opposite sec- 969
 918 tor traversing through the beam pipe. Such tracks 970
 919 are not reconstructed but they are included in the 971
 920 event simulation. Distributions of charged parti- 972
 921 cles in azimuthal angle vs. momentum are shown 973
 922 in Fig. 37. Figure 38 shows the production vertex 974
 923 as reconstructed in the FD tracking system (from 975
 924 data where the FMT was not installed). As the 976
 925 tracking detectors in each sector are independent of 977
 926 each other, they have to be independently aligned 978
 927 and calibrated. The reconstructed vertex is inde- 979
 928 pendent of the sector and also independent of the 980
 929 electron momentum, is an indication that the track- 981
 930 ing detectors are well aligned. 982

931 Neutral particles are detected in either the calorime- 983
 932 ters or in the FTOF (or both). The reconstruction 984
 933 begins by finding isolated clusters of energy, and 985
 934 determining the spatial location, deposited energy, 986
 935 and the time of the cluster. Neutral particle can- 987
 936 didates are identified as clusters in the outer detec- 988
 937 tors (FTOF, PCAL, EC) that do not match any 989
 938 charged particle track. For high-energy photons 990
 939 that deposit all of their energy in the calorimeters, 991
 940 the energy is calculated from the signal pulse height 992
 941 in the calorimeters. The momenta of neutrons are 993
 942 computed from their flight time as determined by 994
 943 the timing signal in the calorimeters and, when rel- 995
 944 evant, the matched FTOF counter. In either case, 996
 945 the angle of the neutral particle trajectory is deter- 997
 946 mined from the position of the cluster at a depth 998

999 in the ECAL that minimizes parallax effects asso- 1000
 1000 ciated with tracks that are not normal to the face 1001
 1001 of the ECAL (see Ref. [15] for details).

1002 For all events, precise determination of the in- 1003
 1003 teraction time or event start time is required. For 1004
 1004 events where the scattered electron is detected, the 1005
 1005 event start time is derived from the arrival time of 1006
 1006 the electron at the FTOF counters, corrected for 1007
 1007 flight path and signal delays. The average time res- 1008
 1008 olution for electrons reconstructed in the CLAS12 1009
 1009 FD is better than 80 ps. A more accurate event 1010
 1010 start time is obtained by replacing the measured 1011
 1011 electron start time with the 499 MHz accelerator 1012
 1012 RF signal (or 249.5 MHz depending on the acceler- 1013
 1013 ator setup) that determines the beam bunch asso- 1014
 1014 ciated with the event. In this way, the event start 1015
 1015 time can be determined to within \sim 20 ps, thus 1016
 1016 eliminating a significant contribution to the time 1017
 1017 resolution smearing for charged hadrons. This ex- 1018
 1018 tends the charged particle identification capabilities 1019
 1019 of CLAS12 towards higher particle momentum.

1020 Track reconstruction in the CD is generally less 1021
 1021 complex as tracks are determined fully by the geom- 1022
 1022 etry of the detection elements and the hit pattern in 1023
 1023 the CVT, i.e. by a combination of the SVT and the 1024
 1024 BMT trackers. In contrast to the charged particle 1025
 1025 tracking in the FD that relies heavily on timing in- 1026
 1026 formation for resolution, this is not the case for the 1027
 1027 CD. In principle, that makes tracking easier in the 1028
 1028 CD. On the other hand, the redundancy of track 1029
 1029 fitting is much reduced in the CD as there are only 1030
 1030 12 tracking layers compared to the 36 in the FD. 1031
 1031 This makes tracking in the CD more susceptible to 1032
 1032 losing tracks due to accidental hits. Charged parti- 1033
 1033 cle identification in the CD is given by the tim- 1034
 1034 ing information in the CTOF (or CND) scintilla- 1035
 1035 tors combined with the track momentum measured 1036
 1036 in the strong solenoid magnetic field.

1037 Neutral particles are detected in the CD in the 1038
 1038 CND or the CTOF (or both). As for the FD, neu- 1039
 1039 tral particle candidates are identified as clusters 1040
 1040 that do not match any charged particle track. See 1041
 1041 Ref. [27] for full details on the CLAS12 offline re- 1042
 1042 construction software architecture and design.

9. CLAS12 Operational Performance

1043 This section describes the overall performance 1044
 1044 of the CLAS12 detection system. Most of the ex- 1045
 1045 perimental programs require the clean identification 1046
 1046 and reconstruction of the scattered electron. Elec- 1047
 1047 trons are identified by a combination of signals in

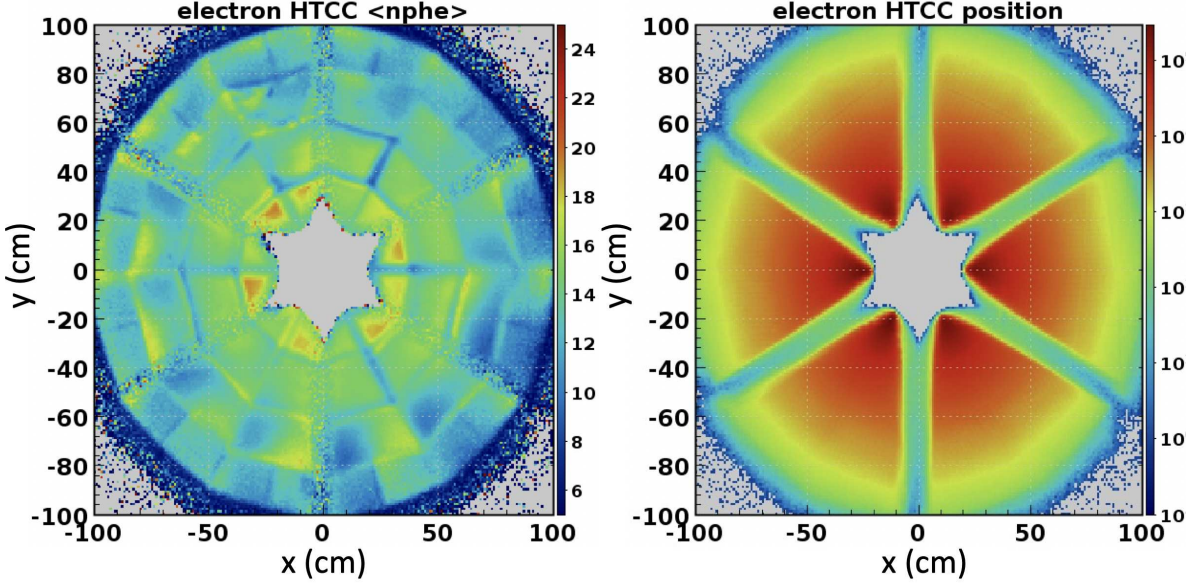


Figure 39: Distribution map of the number of photoelectrons collected in polar and azimuthal angle of the HTCC shown in terms of the y vs. x transverse coordinates. The plot is based on measurements with a trigger threshold of 2 photoelectrons. The averaged electron detection efficiency is estimated at greater than 99% in the full phase space covered by the HTCC. In localized areas, in particular at interfaces of different mirror facets or between mirror sectors, the efficiencies can be as low as 94%. This map enables bin-by-bin corrections for absolute normalization. Right panel: Distribution of electrons from forward tracking reconstruction at the HTCC location in polar and azimuthal angle. The gaps between sectors are due the scattered electrons being lost in the torus coils and not reconstructed.

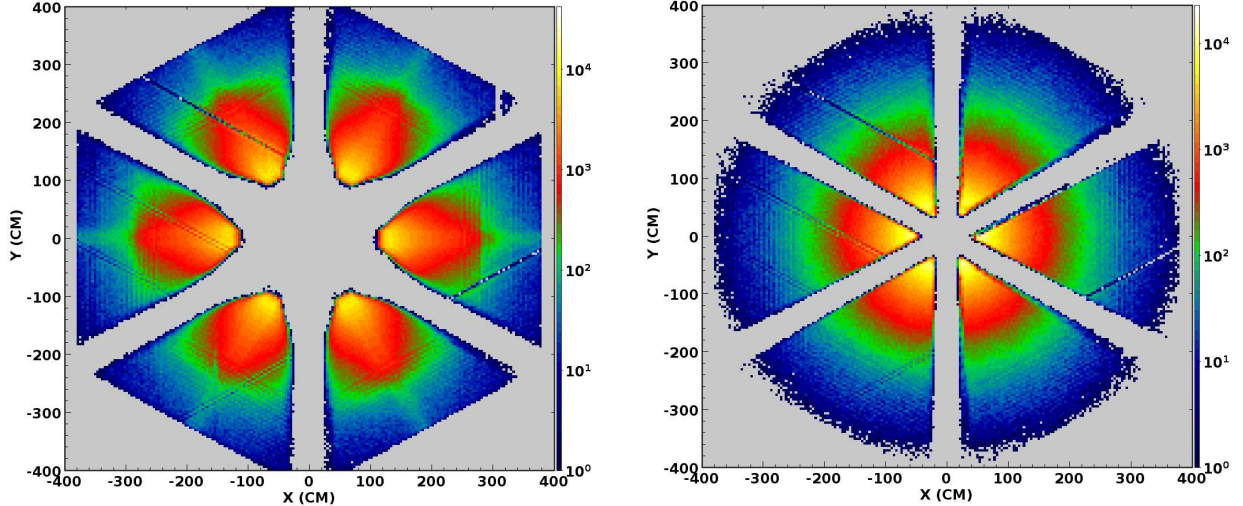


Figure 40: Distribution of electron track y vs. x coordinates propagated to the PCAL front face (as seen from the target). The few empty strips are due to hardware issues. (Left) Data for electrons bent away from the beamline (outbending). Right: Data for electrons bent toward the beamline (inbending).

997 the HTCC and energy deposited in the combined 1001
 998 electromagnetic calorimeters PCAL and EC, with a 1002
 999 matched negatively charged track in the DC track- 1003
 1000 ing system. Of critical importance is the response 1004

of the HTCC that operates between the CD and the entrance to the DC system. The reconstructed electron coordinates at the HTCC are shown in Fig. 39(right), exhibiting a very uniform distribu-

1005 tion in azimuthal angle. The distribution of photo- 1056
 1006 electrons across the entire 48 segments of the HTCC 1057
 1007 active region is shown in Fig. 39(left), which ex- 1058
 1008 hibits a rather uniform and high efficiency for elec- 1059
 1009 trons over its full acceptance.

1010 The coordinates of the reconstructed electrons 1061
 1011 at the front face of the PCAL are shown in Fig. 40 1062
 1012 for electrons bending towards the beamline, and 1063
 1013 with reversed torus magnetic field with electrons 1064
 1014 bending away from the beamline. The different ap- 1065
 1015 pearance of the two plots is the result of the dif- 1066
 1016 ference in optics for the two configurations. The 1067
 1017 distributions are rather uniform in all six sectors, 1068
 1018 showing that the detector systems and the recon- 1069
 1019 struction software are working properly. The few 1070
 1020 empty strips indicate malfunctioning detector ele- 1071
 1021 ments or electronics modules. The acceptances for 1072
 1022 the inbending and the outbending scattered elec- 1073
 1023 tron show quite different features. Outbending elec- 1074
 1024 trons hit the ECAL front face significantly further 1075
 1025 out radially than inbending electrons do. This is a 1076
 1026 feature of the magnetic field of the torus magnet. 1077
 1027 Also, the outer acceptance bounds are quite differ- 1078
 1028 ent. In the outbending case, they are defined by 1079
 1029 the ECAL geometry, while for the inbending case 1080
 1030 the acceptance bounds are given by the HTCC 1081
 1031 geometry, as can be seen in Fig. 39.

1032 Elastic scattering of electrons on protons allows 1082
 1033 for the establishment of any deviations from the 1083
 1034 ideal detector geometry and alignment. The cov- 1084
 1035 erage in kinematical quantities Q^2 and x_B of the 1085
 1036 scattered electrons detected in the FD is shown 1086
 1037 in Fig. 41. Q^2 is the virtuality of the photon ex- 1087
 1038 changed from the electron to the proton target and 1088
 1039 x_B is the Bjorken scaling variable (defined as $Q^2/(2M_{\gamma}E_{\gamma})$) 1089
 1040 where M is the target mass and E_{γ} is the energy 1090
 1041 of the virtual photon exchanged with the target). 1091
 1042 The electron kinematics also define the invariant 1092
 1043 mass W defined as $W^2 = M^2 + 2M\nu - Q^2$, with 1093
 1044 $\nu = E_e - E_{e'}$ and M the mass of the target parti- 1094
 1045 cle. For inbending electrons the coverage in Q^2 is 1095
 1046 up to 13 GeV^2 at $x_B \approx 1$, while for the outbending 1096
 1047 electrons it is limited to $Q^2 \approx 12 \text{ GeV}^2$.

1048 9.1. Charged Particle Detection in the FD

1049 Charged particle yields in momentum and az- 1098
 1050 imuthal angles are shown in Fig. 37 in the local 1099
 1051 sector frame for positively and negatively charged 1100
 1052 particles. The difference in the acceptance is due 1101
 1053 to two factors, the polarity of the torus magnet 1102
 1054 that bends negative particles away from the beam- line and positive particles towards the beamline (or

vice-versa for the opposite torus polarity), and the effects of the solenoid magnetic field that causes an azimuthal motion for positive and negative particles in opposite directions.

1060 Identification of charged particles in CLAS12 is 1061
 1062 achieved in a number of ways. Identified electrons 1063
 1064 are used to determine the hadron start time at the 1065
 1066 production vertex. The start time and the path 1067
 1068 length of charged tracks from the production ver- 1069
 1069 tex to the FTOF and the FTOF hit time, enable 1070
 1070 the determination of the velocity ($\beta = v/c$) of the 1071
 1071 particle, shown in Fig. 42 vs. particle momentum 1072
 1072 for positively charged tracks. The computed mass 1073
 1073 squared vs. momentum for these tracks is shown in 1074
 1074 Fig. 43. An overview of the detector subsystems in 1075
 1075 the CLAS12 FD used for the identification of the 1076
 1076 different charged particle species vs. momentum is 1077
 1077 shown in Fig. 44.

1078 Figure 45 shows the inclusive invariant mass W 1079
 1080 spectra for $ep \rightarrow e'X$ and missing mass spectra for 1081
 1081 $ep \rightarrow e'\pi^+X$ with a missing neutron at four dif- 1082
 1082 ferent beam energies. Figure 46 shows the invariant 1083
 1083 mass of $\pi^+\pi^-$.

9.2. Charged Particle Detection in the CD

1084 Momentum reconstruction in the CVT combined 1085
 1085 with the timing information from the CTOF al- 1086
 1086 lows for the separation of charged pions, kaons, and 1087
 1087 protons in the momentum range from 0.3 GeV to 1.25 1088
 1088 GeV. This momentum range covers a large part 1089
 1089 of the phase space allowed by the maximum beam 1090
 1090 energy for hadron electroproduction on hydrogen 1091
 1091 targets. Figure 47 shows the reconstructed mass 1092
 1092 squared vs. particle momentum reconstructed in 1093
 1093 the CVT.

9.3. Neutral Particle Detection

1094 Direct detection of neutral particles is accom- 1095
 1095 plished in the FD using the PCAL and EC calorime- 1096
 1096 ters. The combined 20 radiation lengths are suf- 1097
 1097 ficient to identify high-energy photons and recon- 1098
 1098 struct the masses of the parent particles, such as 1099
 $\pi^0 \rightarrow \gamma\gamma$ or $\eta \rightarrow \gamma\gamma$. At very forward angles the 1100
 1100 FT provides photon detection with significantly im- 1101
 1101 proved position and energy resolution in the polar 1102
 1102 angle range from 2.5° to 4.5° . Figure 48 shows the 1103
 1103 invariant mass of the $\gamma\gamma$ system in the CLAS12 FD. 1104
 1104 The energy response of the FT to 2.2 GeV electrons 1105
 1105 and the $\gamma\gamma$ mass resolution are shown in Fig. 49.

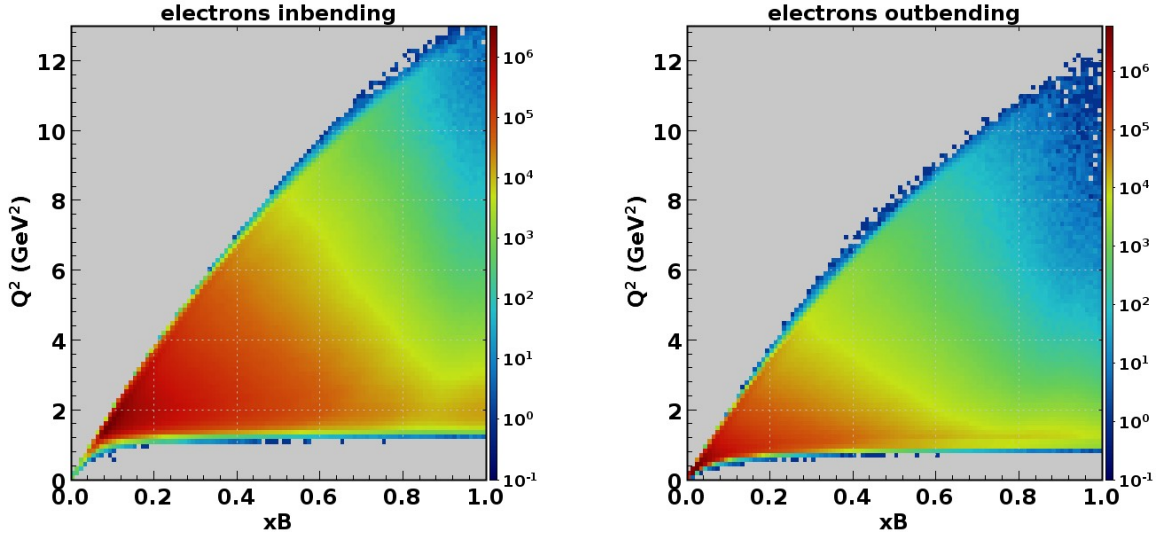


Figure 41: Inclusive $ep \rightarrow e'X$ coverage in Q^2 vs. x_B at a beam energy of 10.6 GeV. The full kinematics is measured simultaneously. The kinematic range is given by elastic scattering kinematics at $x_B = 1$, and the small angle acceptance at the Q^2 limit for scattered electrons bending (left) toward the beamline (inbending) or (right) away from the beamline (outbending). The two configurations require opposite directions of currents in the torus magnet coils. Note that the minimal Q^2 is lower for the electron outbending configuration, and that the maximum Q^2 reach is slightly higher for inbending electrons.

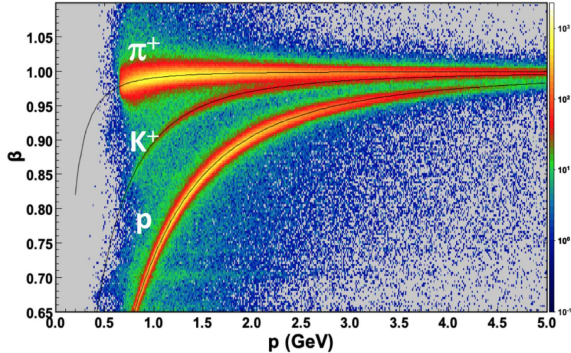


Figure 42: $\beta = v/c$ vs. momentum of positively charged particles detected in the CLAS12 FD. Events were selected to have an electron identified. The charged particle trajectories are reconstructed and their path length and timing from the target to the FTOF (panel-1b layer) are determined. The start time at the target is given by identifying the corresponding beam bucket as time $t=0$. The thin black lines show the expected distributions for the respective charged tracks. Particle identification is limited to momenta greater than 0.8 GeV when the torus magnet is energized to maximum current. At reduced torus current the tracking is extended to lower momenta at the expense of momentum resolution.

Neutral particle detection in the CD is provided by the CND combined with the CTOF. The plastic scintillator bars of the CND have an $\approx 12\%$ nuclear interaction length, resulting in a $\approx 10\%$ ef-

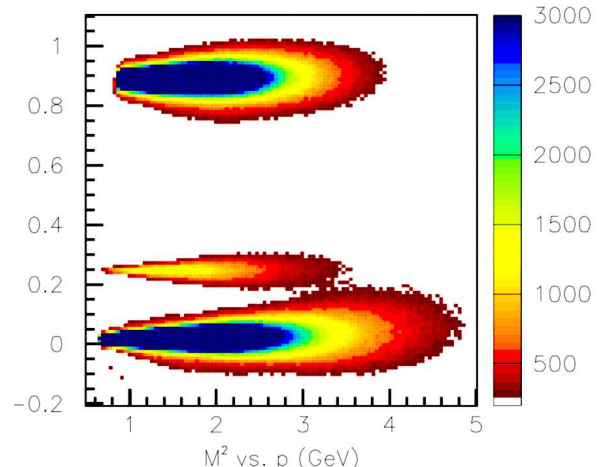


Figure 43: Reconstructed mass squared vs. momentum of positively charged particles in the CLAS12 FD. The same data are used as in Fig. 42. However, the plot contains a threshold on the minimum and maximum number of events per bin to eliminate background events between the particle bands, and to better visualize the scarce kaons in the particle samples, which are of special significance for the science program. Bottom: π^+ , middle: K^+ , top: p . The centroids of each particle distribution are approximately independent of the momentum. Masses are computed from the particle path length and from time-of-flight. Any momentum dependence would indicate systematics in the timing calibration or in the path length determination.

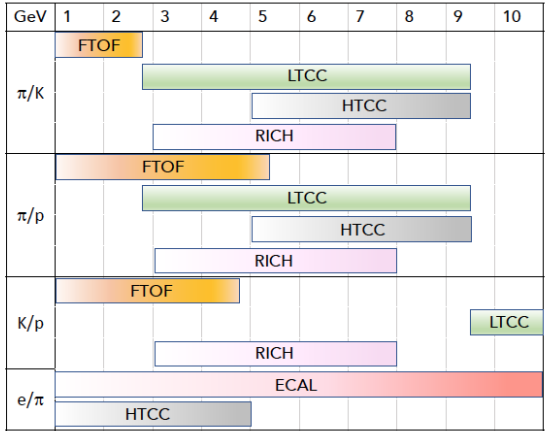


Figure 44: Overview of the different detector subsystems in the CLAS12 FD used for particle species separation vs. momentum. Higher color intensity corresponds to higher sensitivity.

iciency for the detection of high-energy neutrons. The plastic scintillators contribute about 29.6% of a radiation length at $\theta=90^\circ$; hence they also detect high-energy photons through their conversion into e^+e^- pairs. The discrimination of photons and neutrons in the CD is accomplished by the timing resolution of 80 to 100 ps provided by the CTOF and the 160 ps of the CND. The separation of neutral particles from charged particle hits in the CND or in the CTOF is efficiently achieved by using the CVT tracker to veto against false neutral hits in the CTOF and CND. Figure 50 shows the velocity vs. the energy deposition of charged and neutral particles in the CND. The measured neutron detection efficiency is shown in Fig. 51.

At far backward angles, the BAND detector provides neutron identification with detection efficiencies up to 35%. As there are no tracking capabilities in the very backward direction, the separation of charged particles is achieved by a veto counter, corresponding to a 1-cm-thick scintillation counter in front of the BAND. The separation of neutrons and photons is achieved by the timing information, which is shown in Fig. 52.

10. Electron Beam Operation

During beam operation the status of the beamline diagnostics and other critical components, as well as most of the detector components, are continuously monitored. Some of the beamline elements

are used to warn of beam conditions that may negatively impact detector operation and are used as a fast shutdown of beam delivery.

10.1. Forward Detector Reconstruction

The science program with CLAS12 in general requires the detection of electrons that are scattered off the target material. For determining the kinematics of the reaction, the electrons must be identified and their 3-momentum determined by tracking them in the magnetic field of the torus magnet, and detecting them in the FTOF and in the ECAL, which covers approximately the polar angle range from 5° to 35° . The detailed acceptance ranges depend also on the polarity of the torus magnetic field. Charged tracks that are deflected away from the beamline have acceptance functions that are different from charged tracks that are deflected toward the beamline. Figure 53 shows the distribution of reconstructed electrons vs. azimuthal angle ϕ for different ranges of polar angle θ at 8° and 26° showing the different acceptances for outbending vs. inbending electrons.

The magnetic field of the solenoid also affects the acceptance function of charged particles. For opposite charges but the same momentum, the azimuthal rotation of scattered charged particles is the same in magnitude but opposite in sign. The particle acceptance is a complex function of the phase space covered by the processes of interest and must be simulated in full detail to precisely extract cross sections and other physics observables. For this purpose a full simulation package was developed, based on the software package Geant4 [24].

10.1.1. Luminosity Performance During CLAS12 Operations

CLAS12 is designed for operation at a luminosity of $L = 10^{35} \text{ cm}^{-2}\text{s}^{-1}$, which corresponds to a beam current of 75 nA and a liquid-hydrogen target of 5 cm length. The high-luminosity operation has measurable effects on the hit occupancy in the drift chambers and on the resolution in the reconstruction of kinematical quantities. Also, the reconstruction efficiency of charged particles can be affected. Figures 54 and 55 show the hit occupancies in the drift chambers for different beam currents and for different currents in the solenoid magnet, respectively.

The effects of luminosity on the reconstruction can be studied in simulations when the beam conditions can be realistically imposed on the data.

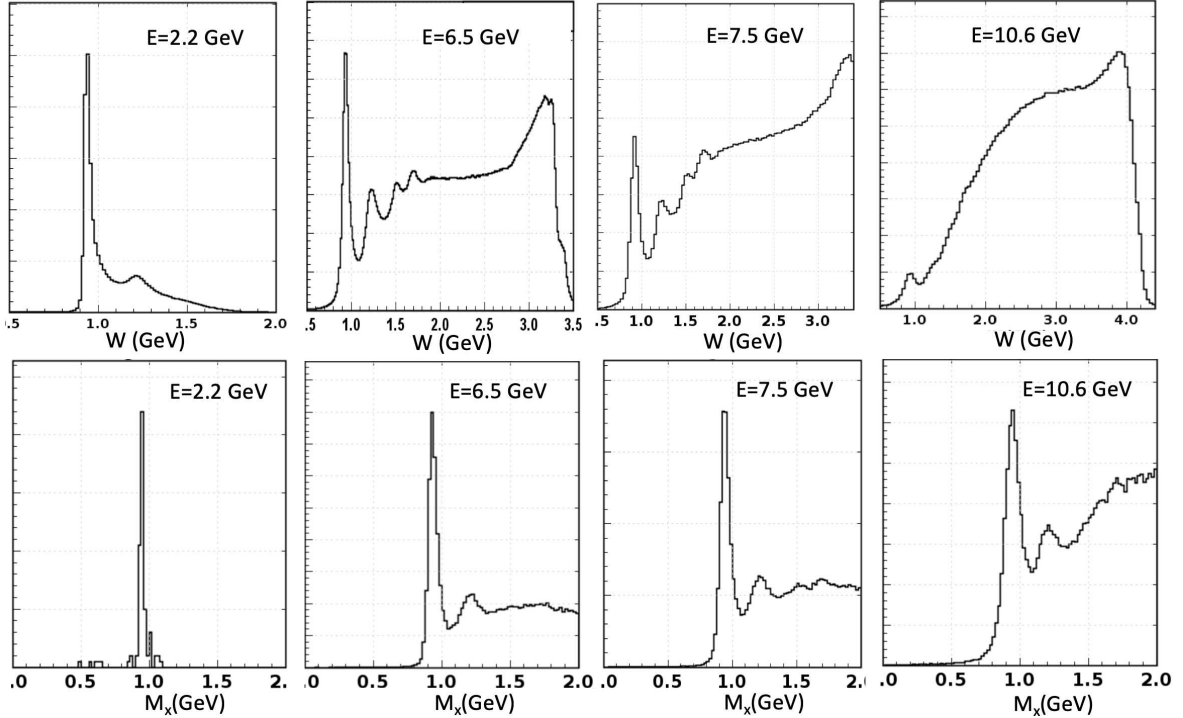


Figure 45: Upper row: Inclusive electron scattering spectrum $ep \rightarrow e'X$ measured in CLAS12 at beam energies of 2.2 GeV, 6.5 GeV, 7.5 GeV, and at 10.6 GeV (from left to right). The peak to the left is due to elastic $ep \rightarrow ep$ scattering. Enhancements from the first 3 excited nucleon states, $\Delta(1232)$, $N(1520)$, and $N(1680)$, are also visible for the lower beam energies. Note that the mass ranges are different for the different beam energies. Lower row: Missing mass distributions of $ep \rightarrow e'\pi^+X$ for the same energies. The sharp mass peak to the left is due to the undetected neutron. The second peak for the higher energies is due to the $\Delta^0(1232)$. Indications of higher mass neutron excitations are also visible.

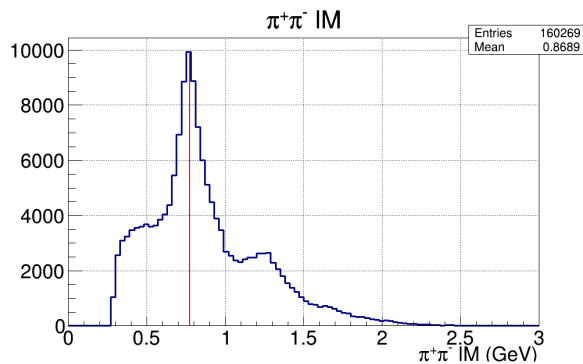


Figure 46: Invariant mass of $\pi^+\pi^-$ at 10.6 GeV beam energy. The vertical line indicates the mass of the $\rho^0(770)$ meson. The shoulder to the right is from the $f_2(1270)$ meson.

For that purpose a procedure was developed that takes randomly triggered events at the operating beam current and superimposes these events on the simulated events without the background. In this way one can study the reconstruction efficiencies

as a function of luminosity of the actual experiment. With increasing luminosity, accidental out-of-time events can affect and alter particle tracks that come in-time. The most important effect is that the track quality is negatively impacted, leading to track losses if stringent quality requirements are applied, or to a worsening of the angle and momentum resolution. This effect is demonstrated in Table 1.

Another way of quantifying the effect of accidental background is by studying the percentage of tracks lost when certain track quality requirements are imposed. Detailed simulations must be done for specific operating conditions, such as magnetic field settings, event triggers, beam current, and production targets. As an illustration, an example of such a simulation is shown in Fig. 56. The process simulated was elastic muon-proton scattering (which, of course is not feasible at an electron accelerator), where the proton mass is inferred from the elastic muon track, and compared with the known proton

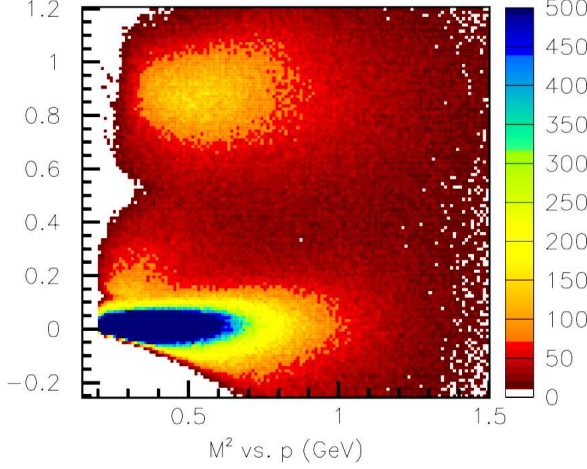


Figure 47: Mass squared of positively charged particles evaluated from their path length and the time-of-flight information in the CTOF vs. the particle momentum at 10.6 GeV beam energy. The band at the bottom is from π^+ , the faint band near 0.2 is from K^+ , and the band at the top is from protons. The momenta are not corrected for energy loss in the CVT.

Parameter	Current	Resolution	Specs
$\Delta p/p$ (%)	0 nA	0.52	≤ 1
	60 nA	0.67	
	120 nA	0.86	
$\Delta\phi$ (mrad)	0 nA	3.3	≤ 4.5
	60 nA	3.8	
	120 nA	4.4	
$\Delta\theta$ (mrad)	0 nA	0.66	≤ 1
	60 nA	0.85	
	120 nA	0.85	
Δv_z (mm)	0 nA	3.5	-
	60 nA	4.6	
	120 nA	5.6	

Table 1: Impact of high-current operation on the resolution of kinematic quantities in single track reconstruction. The resolution parameters are without the use of the FMT tracker, which should significantly improve the v_z -vertex resolution. Note that the highest beam current of 120 nA is 60% higher than the nominal operating value of 75 nA.

mass. Muons were used as an ideal probe that does not require corrections for radiative effects as electron scattering does. At higher beam currents, increasingly wider tails develop on the inferred proton mass.

For the first run period of CLAS12 in the spring and fall of 2018, the luminosity was limited to not exceed average occupancies of 4% in the R1 drift

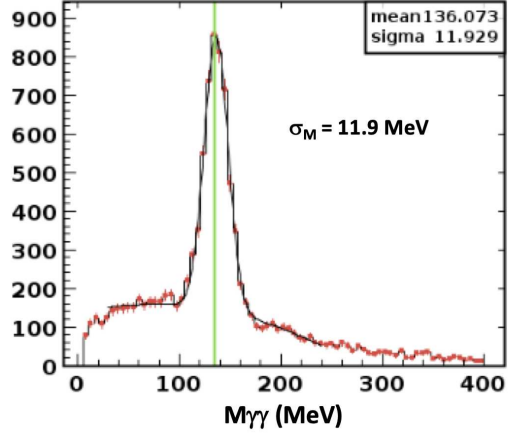


Figure 48: The invariant mass of two high-energy photons in Sector 4 of the ECAL from 10.6 GeV beam data. The background beneath the π^0 peak is due to multi-photon decays of higher-mass mesons where one or more photons are not detected in the angle range covered by the calorimeter. The width (σ) of the mass peak is 11.9 MeV, which is in good agreement with the Monte Carlo simulations in Ref. [27]. The energy calibration of the calorimeter uses cosmic ray muons.

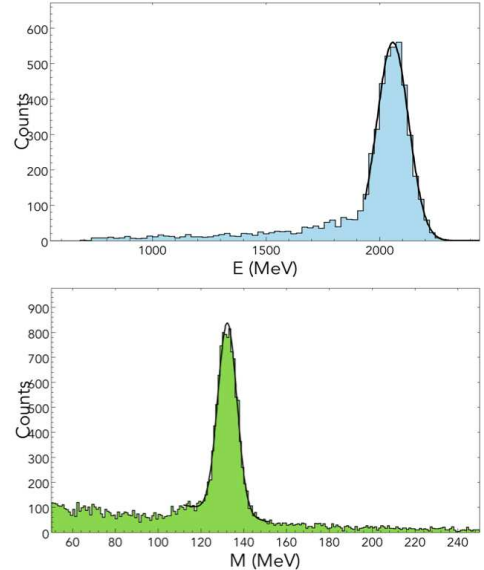


Figure 49: Top: The energy response of the FT calorimeter to elastically scattered electrons at 2.2 GeV beam energy. The tail at lower energies is due to radiative effects. The energy resolution is $\sigma_E/E \approx 3.3\%$. Bottom: 2γ mass for photons detected in the FT lead-tungstate crystal calorimeter. The π^0 mass resolution is $\sigma_{\gamma\gamma} = 4.4$ MeV, which is somewhat larger than the Monte Carlo simulation resolution of ≈ 3.5 MeV.

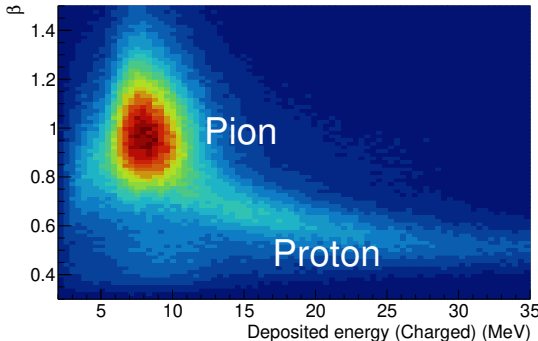


Figure 50: Top: Distribution of $\beta = v/c$ for charged particles in the CND vs. the deposited energy for correlated charged tracks in the CVT. Evidence for charged pions and protons is clearly visible. Bottom: The same for neutral particles; no charged tracks are correlated with the energy deposited in the CND scintillators.

chambers. The R1 detectors are more exposed to background radiation than R2 and R3. This occupancy limitation typically resulted in beam operations at about 45 nA to 55 nA of beam current, or about 60% to 75% of design luminosity.

10.1.2. Performance of the RICH

Figure 57 shows the RICH multi-anode photomultiplier array and a single Cherenkov event for a track with the Cherenkov light detected in the MaPMT array. The performance in event reconstruction is illustrated in Fig. 58 for positively charged particles in the design momentum range from 3 to 8 GeV.

10.2. CD Reconstruction

Figure 59 shows selected charged track events in the CVT. The left panels show the projection to the plane perpendicular to the beamline. In this view, positively charged particles bend clockwise in the

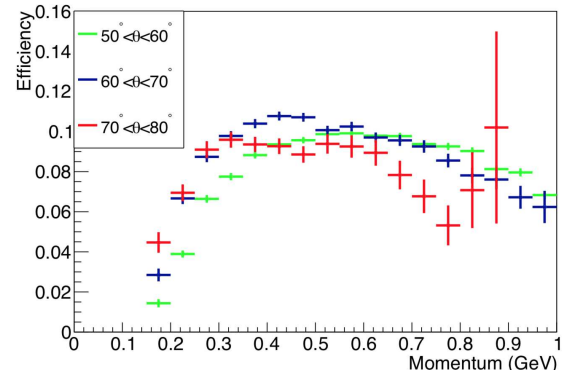


Figure 51: The neutron detection efficiency in the CND vs. momentum for different polar angles. The detection efficiency has been measured using the reaction $ep \rightarrow e' \pi^+ n$, where the neutron kinematics are given by the other detected particles. The ratio of observed neutron hits to predicted neutron hits in the CND gives the detection efficiency. The efficiency has some angle and momentum dependence as shown.

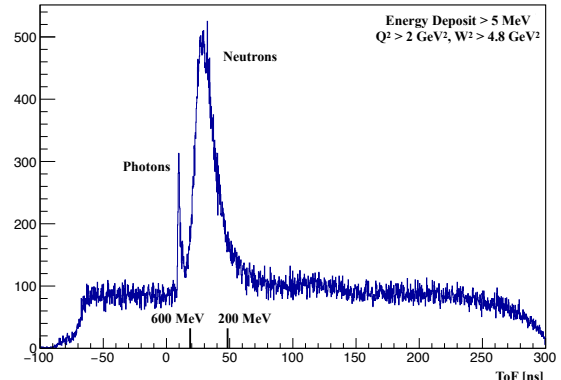


Figure 52: BAND response to electron-triggered events emerging from a nuclear target at very backward polar angles. Photons and neutrons sitting on accidental background events are well separated by precise timing information.

5 T magnetic field. The innermost 3 double layers mark the SVT and the outer 6 layers indicate the BMT. The panels to the right show the projection onto a plane along the beamline. The CTOF and CND detectors are located radially outward of the CVT and also show the deposited energy where the charged tracks hit. Uncorrelated hits are from neutrals or out-of-time events. Other indicators of the

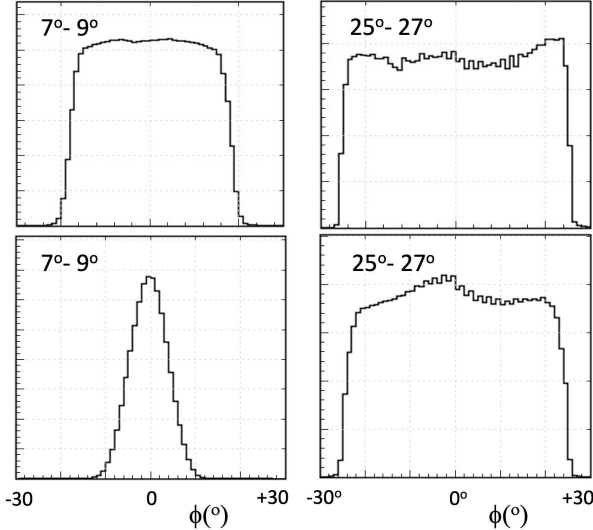


Figure 53: Yields of electrons in azimuthal angle (in deg.) for two bins in polar angle. Top: Outbending electrons, Bottom: Inbending electrons. Left: $\theta = 7^\circ - 9^\circ$. Right: $\theta = 25^\circ - 27^\circ$. The reduced ϕ acceptance at small polar angles is due to the torus coils blocking part of the ϕ coverage, as is seen in Fig. 8). In addition, for inbending electrons the acceptance is further reduced as those electrons bend towards the beamline, where the forward detectors have a smaller extension in azimuth. (The vertical axes are in arbitrary, linear units.)

1246

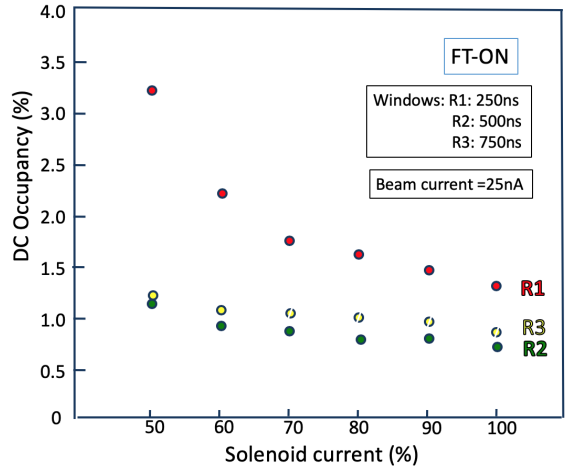


Figure 55: Hit occupancies in the three DC regions vs. the current in the solenoid magnet. The measurement was carried out in the FT-ON configuration. The sensitivity on the solenoid current comes from the fact that the primary background source is from charged particles, especially Møller electrons. The sensitivity is strongest for DC R1, which have no additional magnetic shielding from the torus magnet field, while the R2 and R3 chambers do.

CND performance for charged particles are shown in Fig. 60.

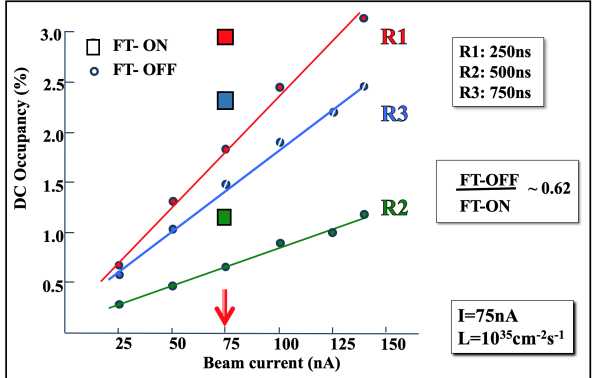


Figure 54: Accidental occupancies in the three DC regions vs. the beam current with the solenoid magnet at full field. The measurement was carried out in the FT-OFF configuration. The dependence on the beam current is linear. At 75 nA beam current the measurement was also done in the FT-ON configuration (large squares), and the accidental occupancies increase on average by $\approx 62\%$ compared to the FT-OFF configuration. The time windows during data collection were 250 ns for R1, 500 ns for R2, and 750 ns for R3, approximately corresponding to the charge collection times in the DC. The FT-ON configuration results are consistent with the Monte Carlo simulations for R1, but they underestimate the R2 data by 35% and the R3 data by 25% [24, 28].

1248
1249
1250
1251
1252
1253
1254
1255
1256
1257
1258
1259
1260
1261
1262
1263
1264
1265
1266
1267
1268
1269
1270
1271
1272

10.2.1. Acceptance and Performance of the CD

The Central Detector system covers polar angles from 35° to 125° and the full 360° in azimuth. Figure 61 shows the acceptance and reconstruction efficiency for charged tracks from simulations with background incorporated according to the beam current. Figure 62 shows the reconstructed vertex along the beamline (z -axis) for charged particles coming from an empty target cell. The target cell is 5-cm long, and the cell walls are well resolved with an approximate resolution of $\sigma_z < 2$ mm. The final vertex resolution should significantly improve with the optimized detector alignment and calibrations. Events between the cell walls are from beam interactions with the residual cold hydrogen gas in the target cell.

The limited space in the CD makes charged particle identification challenging for momenta $\gtrsim 1$ GeV. The current detector performance in terms of particle identification and tracking resolution is still being optimized and improved. It is expected that the results shown here will continue to improve and the performance will become more in agreement with the expected performance parameters.

The elastic scattering process $ep \rightarrow ep$ at rela-

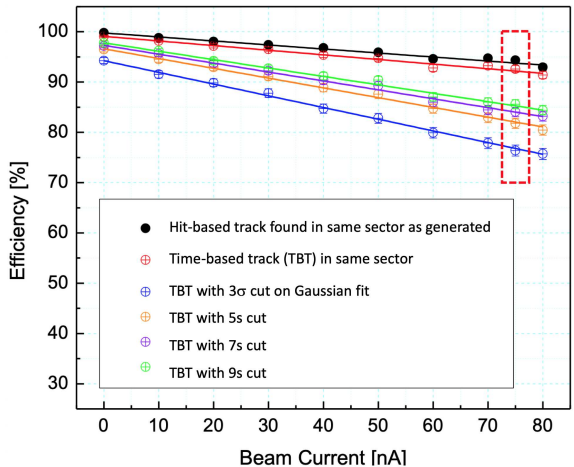


Figure 56: Single track reconstruction efficiency for simulated muon events vs. luminosity. Here the efficiency is defined as the ratio of reconstructed to generated tracks. The accidental background events were used from randomly triggered data runs taken at the same beam current. The different colored points show the tracking efficiency when certain quality constraints are imposed. About 6-7% of the tracks are lost at 75 nA beam current corresponding to a luminosity of $10^{35} \text{ cm}^{-2}\text{s}^{-1}$ with no quality cuts (black: hit-based tracking - HBT, red: time-based tracking - TBT). The other curves show losses in the tracking efficiency when more or less stringent quality cuts are applied on the width of the missing mass distribution. Experimental data will be used to determine realistic tracking efficiencies at different experimental conditions.

tively low Q^2 can be used to connect the FD where the electron is detected and the CD where most of the elastically scattered protons are detected. The strict kinematic correlation in azimuthal angle, given by $\phi_p = \phi_e + 180^\circ$, can be exploited to understand potential relative alignment issues between the FD and CD tracking. Figure 63 illustrates the correlation in elastic electrons detected in the FD sectors and protons reconstructed in the CD.

10.3. Operating Experience

The CLAS12 detector systems were commissioned in the period from December 2017 through February 2018, using beam energies of 2.2, 6.4, and 10.6 GeV. The target cells was filled with liquid hydrogen, except when data were taken on an empty target cell. Data were accumulated with both torus magnet polarities, i.e. electrons bending either toward or away from the beamline, as well as data with different magnetic field strength settings in the torus and solenoid. Understanding of the reconstructed events focused first on the lowest beam energy of

2.2 GeV, for which the elastic peak became quickly visible and could be used to understand the influence of the magnetic field map, the overall detector geometry, and the drift chamber alignment, among other parameters. Figure 64 shows the elastic electrons detected in each of the six different sectors of the FD to illustrate that quality of the event reconstructions and detector calibrations. After this initial commissioning period, data taking commenced for Run Group A [29], which required use of a liquid-hydrogen target. Use of hydrogen as the target material allowed for the continuation of the commissioning period, while taking production data at the same time. The ability to study exclusive processes plays an essential role in further optimizing the operational performance.

11. Summary

The design criteria, construction details, and operational performance characteristics of the large-acceptance CLAS12 dual-magnet spectrometer in Hall B at Jefferson Laboratory have been described. The spectrometer is now used to study electron-induced reactions at the energy-doubled CEBAF electron accelerator. The spectrometer was commissioned in the period from late 2017 to early 2018, and is now routinely operated in support of a diverse scientific program in the exploration of the internal quark structure of nucleons and nuclei. The major performance criteria, most critically, the operation at instantaneous luminosities up to $10^{35} \text{ cm}^{-2}\text{s}^{-1}$, have been met. These criteria are summarized in Table 2. Further improvements in the operational performance of CLAS12 will be realized during the ongoing experimental data analysis and detector optimization studies.

Acknowledgments

We acknowledge the outstanding efforts of the staff of the Accelerator and the Nuclear Physics Division at JLab that have contributed to the design, construction, installation, and operation of the CLAS12 detector. This work was supported by the United States Department of Energy under JSA/DOE Contract DE-AC05-06OR23177. This work was also supported in part by the U.S. National Science Foundation, the State Committee of Science of the Republic of Armenia, the Chilean

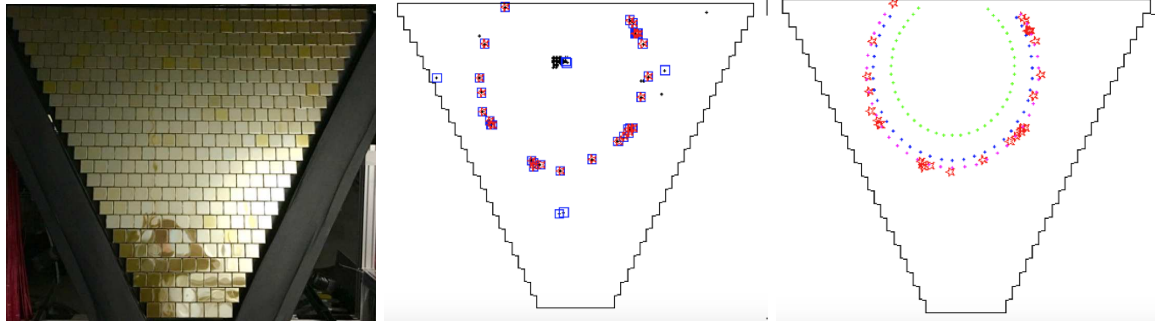


Figure 57: Photograph (left) and detector response (right) of the RICH MaPMT array during beam operation. Middle: One event with the ring of Cherenkov photons. Right: same event overlaid with expected rings from a pion, kaon, and proton at the same momentum. The radius of the Cherenkov ring is consistent with the outermost circle, which corresponds to a pion.

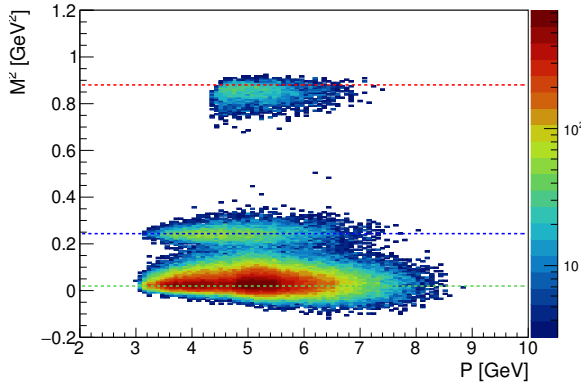


Figure 58: Charged particle identification in the RICH detector showing the mass squared vs. momentum for positively charged particles. The data show bands for π^+ (bottom), K^+ (middle), and protons (top). The events are from a single aerogel tile, and from photons that hit the MAPMT directly, without reflection from the mirrors. The pion/kaon separation in the RICH sets in where it ranges out with the time-of-flight resolution in the FTOF shown in Fig. 42.

1340 Comisión Nacional de Investigación Científica y Tec-
 1341 nológica, the Italian Istituto Nazionale di Fisica Nu-
 1342 cleare, the French Centre National de la Recherche
 1343 Scientifique, the French Commissariat a l'Energie
 1344 Atomique, the Scottish Universities Physics Alliance
 1345 (SUPA), the United Kingdom Science and Tech-
 1346 nology Facilities Council (STFC), the National Re-
 1347 search Foundation of Korea, the Deutsche Forschungs-
 1348 gemeinschaft (DFG), and the Russian Science Foun-
 1349 dation.

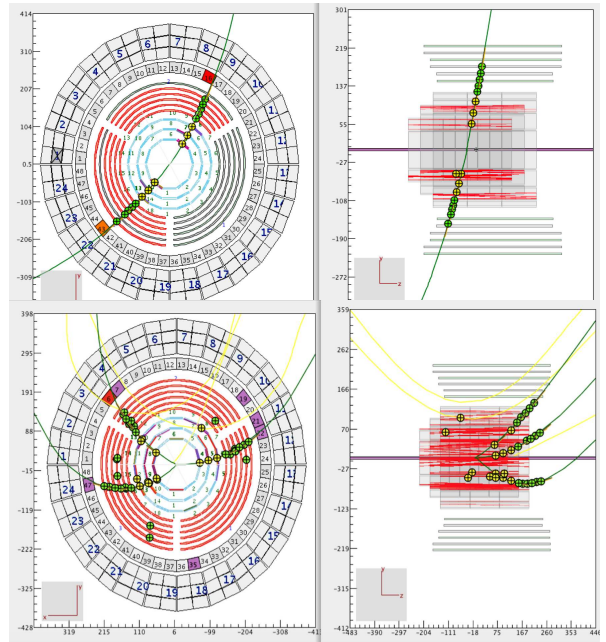


Figure 59: Top: Example of cosmic ray tracks in the CVT with magnetic field $B = 5$ T. Left: Track projected to the plane perpendicular to the beamline. Right: The same track projected onto a plane along the beamline. Bottom: Multiple track event from beam-target interaction reconstructed in the CLAS12 Central Detector at a beam current of 10 nA. Clockwise bending tracks in the solenoid magnetic field are from positively charged particles.

Capability	Quantity	Status
Coverage & Efficiency	Tracks (FD)	$5^\circ < \theta < 35^\circ$
	Tracks (CD)	$35^\circ < \theta < 125^\circ$
	Momentum (FD & CD)	$p > 0.2 \text{ GeV}$
	Photon angle (FD)	$5^\circ < \theta < 35^\circ$
	Photon angle (FT)	$2.5^\circ < \theta < 4.5^\circ$
	Electron detection (HTCC)	$5^\circ < \theta < 35^\circ, 0^\circ < \phi < 360^\circ$
	Efficiency	$\eta > 99\%$
	Neutron detection (FD)	$5^\circ < \theta < 35^\circ$
	Efficiency	$\leq 75\%$
Resolution	Neutron detection (CD)	$35^\circ < \theta < 125^\circ$
	Efficiency	10%
	Neutron Detection (BAND)	$155^\circ < \theta < 175^\circ$
	Efficiency	35%
	Momentum (FD)	$\sigma_p/p = 0.5 - 1.5\%$
	Momentum (CD)	$\sigma_p/p < 5\%$
Operation	Pol. angles (FD)	$\sigma_\theta = 1 - 2 \text{ mrad}$
	Pol. angles (CD)	$\sigma_\theta = 10 - 20 \text{ mrad}$
	Azim. angles (FD)	$\sigma_\phi < 1 \text{ mrad}/\sin \phi$
	Azim. angles (CD)	$\sigma_\phi < 1 \text{ mrad}$
	Timing (FD)	$\sigma_T = 60 - 110 \text{ ps}$
	Timing (CD)	$\sigma_T = 80 - 100 \text{ ps}$
DAQ	Energy (σ_E/E) (FD)	$0.1/\sqrt{E} \text{ (GeV)}$
	Energy (σ_E/E) (FT)	$0.03/\sqrt{E} \text{ (GeV)}$
Operation	Luminosity	$L = 10^{35} \text{ cm}^{-2}\text{s}^{-1}$
DAQ	Data Rate	20 kHz, 800 MB/s., L.T. 95%
Magnetic Field	Solenoid	$B_0 = 5 \text{ T}$
	Torus	$\int B dl = 0.5 - 2.7 \text{ Tm at } 5^\circ < \theta < 25^\circ$

Table 2: CLAS12 performance parameters based on the current state of the reconstruction, subsystem calibrations, knowledge of the detector misalignments, and the understanding of the torus and solenoid magnetic fields.

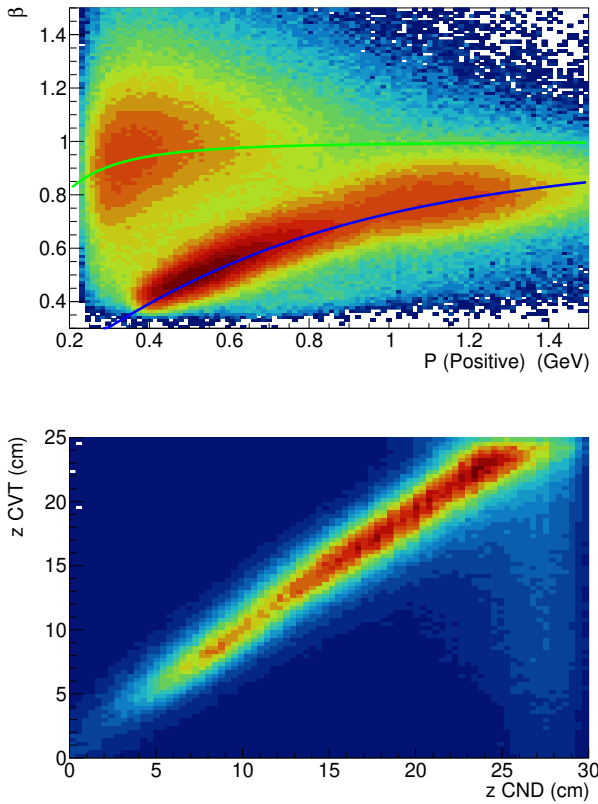


Figure 60: CND response to charged particles. The upper plot shows β vs. particle momentum for positively charged tracks. The green line indicates the nominal relation for pions and the blue line indicates the nominal relation for protons. The bottom plot shows the correlation of the hit position of charged tracks measured in the CVT and the hit position measured in the CND using the hit time information.

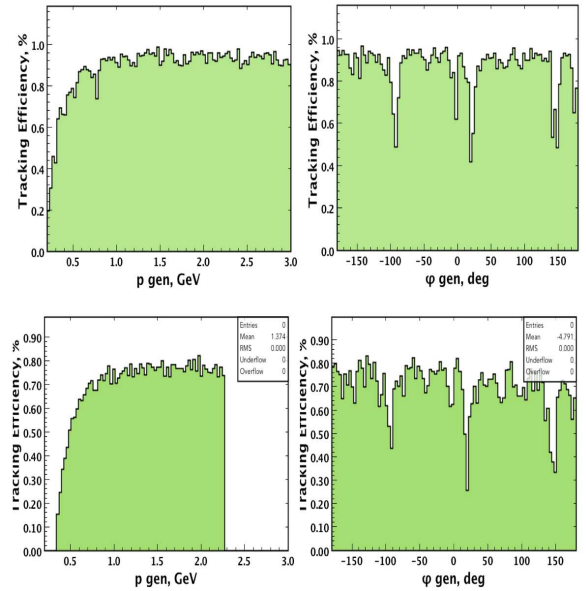


Figure 61: CVT acceptance and tracking performance. The left panels show the tracking efficiency and acceptances vs. momentum for (top) simulated muon tracks with no beam background and (bottom) the same for protons but with background corresponding to a 50 nA beam current. The right plots show the same quantities vs. azimuthal angle. The 3ϕ angle dips are due to the support structure separating the 3 BMT segments, and are thus acceptance related. There are also small acceptance gaps between neighboring SVT modules that may account for some acceptance losses as well.

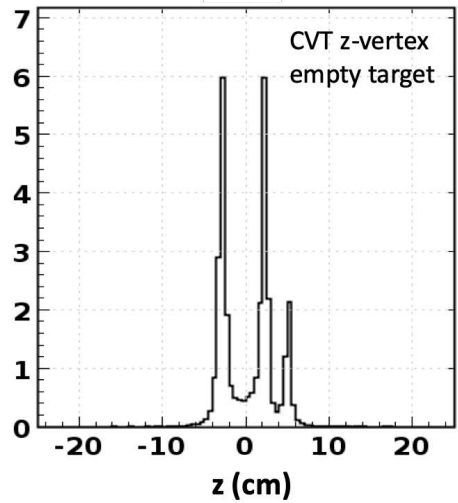


Figure 62: Reconstructed z -vertices (coordinate along the beamline) for charged tracks in the CD from an empty target cell. The cell walls are clearly visible. The small downstream peak at $z \sim 5$ cm is from events originating in a thin thermal shielding foil.

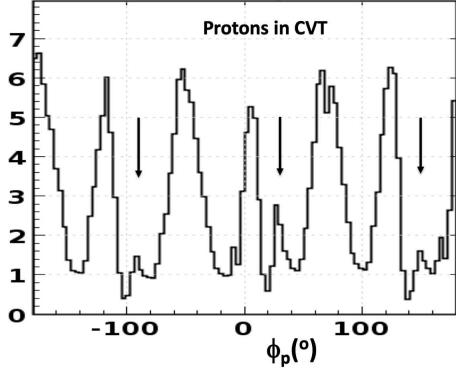


Figure 63: Elastically scattered protons reconstructed in the CVT and CTOF. The proton peaks show the reflection of the 6 FD sectors where the electrons are detected. In addition there is a 3-fold modulation (seen in the different widths of 3 of the peaks) due to the 3 BMT sectors where protons are detected. The arrows indicate the physical position of the support structures at the boundaries between two BMT segments. The azimuthal angle is the reconstructed angle at the production target. Due to the clockwise curvature of proton tracks in the solenoid magnetic field (see bottom plot in Fig. 59) the support structures appear shifted by a certain $\Delta\phi_p$ amount relative to their locations in the lab. (The vertical axes is in arbitrary units).

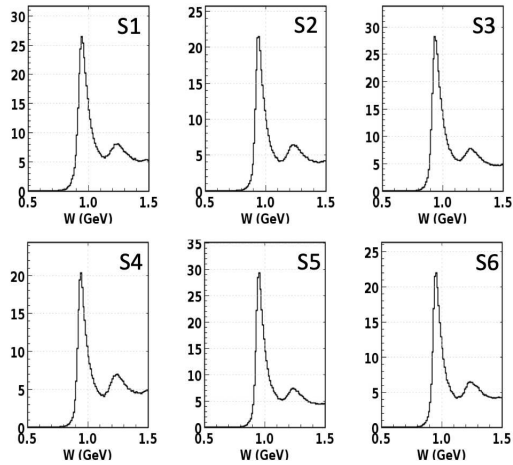


Figure 64: Elastically scattered electrons off protons from 2.2 GeV data in all of the FD sectors showing the reconstructed W distributions.

- 1350 **References**
- 1351 [1] R. W. McAllister and R. Hofstadter, “*Elastic Scat-* 1414
 1352 *tering of 188-MeV Electrons From the Proton and* 1415
 1353 *the α Particle*”, Phys. Rev. **102**, 851 (1956). 1417
 1354 doi:10.1103/PhysRev.102.851 1418
 1355 [2] M. Breidenbach *et al.*, “*Observed Behavior of Highly* 1419
 1356 *Inelastic electron-Proton Scattering*”, Phys. Rev. Lett. 1420
 1357 **23**, 935 (1969). doi:10.1103/PhysRevLett.23.935 1421
 1358 [3] S. E. Kuhn, J.-P. Chen, and E. Leader, “*Spin* 1422
 1359 *Structure of the Nucleon - Status and Recent Re-* 1423
 1360 *sults*”, Prog. Part. Nucl. Phys. **63**, 1 (2009) 1424
 1361 doi:10.1016/j.ppnp.2009.02.001. 1425
 1362 [4] C. W. Leemann, D. R. Douglas, and G. A. Krafft, 1426
 1363 “*The Continuous Electron Beam Accelerator Fa-* 1427
 1364 *cility: CEBAF at the Jefferson Laboratory*”, 1428
 1365 Ann. Rev. Nucl. Part. Sci. **51**, 413 (2001). 1429
 1366 doi:10.1146/annurev.nucl.51.101701.132327 1430
 1367 [5] B. A. Mecking *et al.*, “*The CEBAF Large Acceptance* 1431
 1368 *Spectrometer (CLAS)*”, Nucl. Instrum. Meth. A **503** 1432
 1369 (2003). doi:10.1016/S0168-9002(03)01001-5 1433
 1370 [6] V. D. Burkert, “*Jefferson Lab at 12 GeV: The Science* 1434
 1371 *Program*”, Ann. Rev. Nucl. Part. Sci. **68**, 405 (2018). 1435
 1372 doi:10.1146/annurev-nucl-101917-021129 1436
 1373 [7] R. Fair *et al.*, “*The CLAS12 Superconducting Mag-* 1437
 1374 *nets*”, to be published in Nucl. Inst. and Meth. A, 1438
 1375 (2020). (see this issue) 1439
 1376 [8] M.D. Mestayer *et al.*, “*The CLAS12 Drift Chamber* 1440
 1377 *System*”, to be published in Nucl. Inst. and Meth. A, 1441
 1378 (2020). (see this issue) 1442
 1379 [9] Y.G. Sharabian *et al.*, “*The CLAS12 High Threshold* 1443
 1380 *Cherenkov Counter*”, to be published in Nucl. Inst. and 1444
 1381 Meth. A, (2020). (see this issue) 1445
 1382 [10] G. Adams *et al.*, “*The CLAS Cherenkov detec-* 1446
 1383 *tor*”, Nucl. Instrum. Meth. A **465**, 414 (2001). 1447
 1384 doi:10.1016/S0168-9002(00)01313-9 1448
 1385 [11] M. Ungaro *et al.*, “*The CLAS12 Low Threshold* 1449
 1386 *Cherenkov Counter*”, to be published in Nucl. Inst. and 1450
 1387 Meth. A, (2020). (see this issue) 1451
 1388 [12] M. Contalbrigo *et al.*, “*The CLAS12 Ring Imaging* 1452
 1389 *Cherenkov Detector*”, to be published in Nucl. Inst. and 1453
 1390 Meth. A, (2020). (see this issue) 1454
 1391 [13] D.S. Carman *et al.*, “*The CLAS12 Forward Time-of-* 1455
 1392 *Flight System*”, to be published in Nucl. Inst. and Meth. 1456
 1393 A, (2020). (see this issue) 1457
 1394 [14] M. Amarian *et al.*, “*The CLAS Forward Electromag-* 1458
 1395 *netic Calorimeter*”, Nucl. Instrum. Meth. A **460**, 239 1459
 1396 (2001). doi:10.1016/S0168-9002(00)00996-7 1460
 1397 [15] G. Asryan *et al.*, “*The CLAS12 Forward Electromag-* 1461
 1398 *netic Calorimeter*”, to be published in Nucl. Inst. and 1462
 1399 Meth. A, (2020). (see this issue) 1463
 1400 [16] A. Acker *et al.*, “*The CLAS12 Forward Tagger*”, to be 1464
 1401 published in Nucl. Inst. and Meth. A, (2020). (see this 1465
 1402 issue) 1466
 1403 [17] M. A. Antonioli *et al.*, “*The CLAS12 Silicon Vertex* 1467
 1404 *Tracker*”, to be published in Nucl. Inst. and Meth. A, 1468
 1405 (2020). (see this issue) 1469
 1406 [18] F. Bossu *et al.*, “*The CLAS12 Micromegas Vertex* 1470
 1407 *Tracker*”, to be published in Nucl. Inst. and Meth. A, 1471
 1408 (2020). (see this issue) 1472
 1409 [19] V. Baturin *et al.*, “*Dynamic magnetic shield for* 1473
 1410 *the CLAS12 central TOF detector photomultiplier* 1474
 1411 *tubes*”, Nucl. Instrum. Meth. A **664** (2012)11, 1475
 1412 doi:10.1016/j.nima.2011.10.003 1476
 1413 [20] D.S. Carman *et al.*, “*The CLAS12 Central Time-of-* 1477
 1414 *Flight System*”, to be published in Nucl. Inst. and Meth. 1478
 1415 A, (2020). (see this issue) 1479
 1416 [21] P. Chatagnon *et al.*, “*The CLAS12 Central Neutron* 1480
 1417 *Detector*”, to be published in Nucl. Inst. and Meth. A, 1481
 1418 (2020). (see this issue) 1482
 1419 [22] The CLAS12 Back Angle Neutron Detector (BAND), 1483
 1420 NIM article in preparation. 1484
 1421 [23] N. Baltzell *et al.*, “*The CLAS12 Beamlne and its Per-* 1485
 1422 *formance*”, to be published in Nucl. Inst. and Meth. A, 1486
 1423 (2020). (see this issue) 1487
 1424 [24] M. Ungaro *et al.*, “*The CLAS12 Geant4 Simulation*”, 1488
 1425 to be published in Nucl. Inst. and Meth. A, (2020). (see 1489
 1426 this issue) 1490
 1427 [25] S. Boyarinov *et al.*, “*The CLAS12 Data Acquisition* 1491
 1428 *System*”, to be published in Nucl. Inst. and Meth. A, 1492
 1429 (2020). (see this issue) 1493
 1430 [26] B. Raydo *et al.*, “*The CLAS12 Trigger System*”, to be 1494
 1431 published in Nucl. Inst. and Meth. A, (2020). (see this 1495
 1432 issue) 1496
 1433 [27] V. Ziegler *et al.*, “*The CLAS12 Software Framework* 1497
 1434 *and Event Reconstruction*”, to be published in Nucl. 1498
 1435 Inst. and Meth. A, (2020). (see this issue) 1499
 1436 [28] V. Burkert, S. Stepanyan, J. A. Tan, and M. Ungaro, 1500
 1437 CLAS12 Note 2017-018, (2017). 1501
 1438 [https://misportal.jlab.org/mis/physics/clas12/](https://misportal.jlab.org/mis/physics/clas12/viewFile.cfm/2017-018.pdf?documentId=54) 1502
 1439 viewFile.cfm/2017-018.pdf?documentId=54. 1503
 1440 [29] CLAS12 Run Groups, https://www.jlab.org/Hall-B/clas12-web/Hall_B_experiment_run-groups.pdf 1504